Supporting Information

Photochemical engineering unsaturated Pt islands on the supported Pd nanocrystals for robust pH-universal hydrogen evolution reaction

Yidan Liu [a,b], Nuttapon Yodsin [c], Ting Li [a,d], Haocheng Wu [a], Rongrong Jia [a], Liyi Shi [a,*], Zhuangchai Lai [e,*], Supawadee Namuangruk [a,f,*], and Lei Huang [a,*]

[a] *Research Center of Nano Science and Technology, College of Sciences, Shanghai University, Shanghai 200444, People's Republic of China.*

[b] *College of Textile Science and Engineering (International Institute of Silk), Zhejiang Sci-Tech University, Hangzhou 310018, People's Republic of China.*

[c] *Department of Chemistry, Faculty of Science, Silpakorn University, Nakorn Pathom 73000, Thailand.*

[d] *Jiangxi Province Key Laboratory of Polymer Preparation and Processing, School of Physical Science and Intelligent Education, Shangrao Normal University, Shangrao 334001, People's Republic of China.*

[e] *Department of Applied Physics, The Hong Kong Polytechnic University, Hong Kong SAR, People's Republic of China.*

[f] *National Nanotechnology Center (NANOTEC), National Science and Technology Development Agency (NSTDA), Pathum Thani 12120, Thailand.*

* Corresponding authors.

E-mail addresses: shiliyi@shu.edu.cn (L. Shi); zhuangchai.lai@polyu.edu.hk (Z. Lai); supawadee@nanotec.or.th (S. Namuangruk); leihuang@shu.edu.cn (L. Huang)

Table of Content

Experimental materials and methods

Chemicals. Tetraamminepalladium(II) dichloride ($Pd(NH_3)_4Cl_2 \cdot H_2O$, T100488, ≥ 99%) was purchased from Aladdin. Chloroplatinic acid hexahydrate ($H_2PtCl_6 \cdot 6H_2O$, ≥ 99.9%), concentrated sulfuric acid (H_2SO_4, guaranteed reagent, 98%), hydrogen peroxide (H_2O_2, 30%), phosphoric acid (H_3PO_4, 85%), hydrochloric acid (HCl, 35~37%), absolute methanol (MeOH), potassium hydroxide (KOH, 99.5%) and other chemicals were of analytical grade and purchased from Sinopharm Chemical Reagent Company (Shanghai, China). Titanium (IV) oxide (TiO_2) (Rutile, particle size < 100 nm), commercial Pt/C (20 wt% Pt) dipotassium hydrogenphosphate (K_2HPO_4, 99.5%), monopotassium phosphate (KH_2PO_4, 99.5%), sodium chloride (NaCl, 99.5%) and Nafion solution (5.0 wt %) were purchased from Sigma-Aldrich. High purity flake graphite (XFNANO, XF010-1) was purchased from XFNANO. The ultrapure water (18.25 MΩ·cm) was used in all experiments. All chemicals were used as received without further purification.

Preparation of GO solution.[1,2] Graphene oxide (GO) was prepared according to the improved Hummers' method. In the optimized preparation process, a mixed solution of H_2SO_4 and H_3PO_4 with a volume ratio of 120:13.33 mL was added in a three-necked flask containing 1.0 g graphite flakes in an ice bath, followed by the slow addition of 6.0 g $KMnO_4$. Subsequently, the temperature of bath was raised to 50 °C and stirred continuously for 12 h. Following this, added 150.0 mL ultrapure (UP) water including 1.5 mL H_2O_2 (30%), washed with 5%vol HCl solution and then centrifuged at 12000 rpm for 15 min, removed the supernatant after centrifugation, added UP water to wash and centrifuge at 12000 rpm for 15 min again and repeated three times. The solid was vacuum-dried at 60 °C and then dispersed in UP water to obtain GO solution.

Synthesis of TiO_2-rGO-Pd_7@Pt_3. TiO_2-rGO-Pd_7@Pt_3 was synthesized through a photochemical deposition method. 2.0 mg TiO_2 was dispersed in 250.0 mL of ultrapure water (UP) and ultrasonicated for 10 min. Then added 3.75 mL GO solution (8.0 mg/mL)

and 20.0 mL absolute methanol, forming TiO_2-GO. Magnetic stirred and purged with argon continuously throughout the whole preparation process. The mixed solution in the photoreactor irradiated with a mercury lamp (130 V*4 A) W (130 mW/cm^2) for 15 min, forming TiO_2-rGO (1). Turned off the lamp after the first run of irradiation, 630.0 μL $Pd(NH_3)_4Cl_2 \cdot H_2O$ (1.0 g/100 mL) (2.49 mg Pd element, equivalent of 7.0 wt% Pd loading) was added and the solution then was irradiated for the second run with a light source of mercury lamp (130 V*5.5 A) W (235 mW/cm^2) for 30 min. TiO_2-rGO-Pd_7 seeds were formed on rGO.[3] Turned off the lamp after the step 2 irradiation, 286.6 μL $H_2PtCl_6 \cdot 6H_2O$ (1.0 g/100 mL) (1.07 mg Pt element, equivalent of 3.0 wt% Pt loading) was added and continue the illumination with a mercury lamp (130 V*6 A) W (265 mW/cm^2) for 30 min for the third run. Finally, to ensure the complete transformation of rGO, it was irradiated with a light source of mercury lamp (130 V*8 A) W (360 mW/cm^2) for 90 min for the fourth run. The resulting black solid in suspension was collected by filtering, washing and drying.

Synthesis of TiO_2-rGO-Pd_7@$Pt_{3\text{-}U}$. When reducing the amount of sacrificial reagent absolute methanol, Pd_7@Pt_3 changes from layer-island growth mode to the layered growth mode of Pd_7@$Pt_{3\text{-}U}$. The process of TiO_2-rGO-Pd_7@$Pt_{3\text{-}U}$ preparation is the same as TiO_2-rGO-Pd_7@Pt_3, only the content of absolute methanol was 10.0 mL.

Synthesis of TiO_2-rGO-Pd_7@Pt_1. The process of TiO_2-rGO-Pd_7@Pt_1 preparation is the same as TiO_2-rGO-Pd_7@Pt_3, only the content of $Pd(NH_3)_4Cl_2 \cdot H_2O$ (1.0 g/100 mL) is changed to 620.0 μL (2.45 mg Pd element, equivalent of 7 wt% Pd loading) and the content of $H_2PtCl_6 \cdot 6H_2O$ (1.0 g/100 mL) is changed to 94.0 μL (0.35 mg Pt element, equivalent of 1 wt% Pt loading).

Synthesis of TiO_2-rGO-Pd_7@Pt_5. The process of TiO_2-rGO-Pd_7@Pt_5 preparation is the same as TiO_2-rGO-Pd_7@Pt_3, only the content of $Pd(NH_3)_4Cl_2 \cdot H_2O$ (1.0 g/100 mL) is changed to 644.5 μL (2.55 mg Pd element, equivalent of 7 wt% Pd loading) and the content of $H_2PtCl_6 \cdot 6H_2O$ (1.0 g/100 mL) is changed to 488.3 μL (1.82 mg Pt element, equivalent of 5 wt% Pt loading).

Synthesis of TiO_2-rGO-Pd. On the basis of **TiO_2-rGO-Pd_7 seeds**, the reaction was continued under the irradiation of mercury lamp (130 V*6 A) W (265 mW/cm^2) for 30 min and (130 V*8 A) W (360 mW/cm^2) for 90 min to compare HER performance.

Synthesis of TiO_2-rGO-Pt. 2.0 mg TiO_2 was dispersed in 250mL of ultrapure water (UP) and ultrasonicated for 15 minutes. Then added 3.75 mL GO solution (8 mg/mL). Magnetic stirred and purged with argon continuously throughout the whole preparation process. The mixed solution in the photoreactor irradiated with a mercury lamp (130 V*4 A) W (130 mW/cm^2) for 15 min. Turned off the lamp after the irradiation, 955.3 μL $H_2PtCl_6 \cdot 6H_2O$ (1.0 g/100 mL) (3.56 mg Pt element, equivalent of 10 wt% Pt loading) was added and continue the illumination with a mercury lamp (130 V*4 A) W (130 mW/cm^2) for 30 min. Finally, to ensure the complete transformation of rGO, it was irradiated with a light source of mercury lamp (130 V*6 A) W (265 mW/cm^2) for 30 min and (130 V*8 A) W (360 mW/cm^2) for 90 min. The black solid in suspension was collected by filtering and configured as comparison catalyst.

Characterizations. The transmission electron microscopy (TEM) and High-resolution TEM (HRTEM) characterizations were performed on a JEOL JEM-2010F, 2100F and spherical aberration corrected Transmission Electron Microscope (ACTEM) operated at the accelerating voltage of 200 kV. High-angle annular dark-field scanning transmission electron microscope (HAADF-STEM) and energy dispersive spectroscopy (EDS) elemental mapping images were carried out on a JEM-ARM 300F GRAND ARM equipped with JEOL Cs correctors and Gatan GIF Continuum K3 system, operated at an accelerating voltage of 300 kV and analyzed by Oxford X-ray microanalysis. The X-ray diffraction (XRD) patterns were recorded using X-ray diffractometer with Kα1 radiation (Rigaku smartlab) operated at 9 kW (Rated tube voltage-current are 20-45 kV and 10-200 mA) and a secondary beam graphite monochromator from 10° to 90° (2θ), sweep at 10°/min. X-ray photoelectron spectroscopy (XPS) measurements were conducted using the K-Alpha+ XPS system (Thermo Kalpha; Thermo ESCALAB 250XI; Axis Ultra DLD Kratos AXIS SUPRA; PHI-5000versaprobeIII). The X-ray source of Al Kα radiation was used. The XPS data

were internally standardized with respect to the C 1s peak position at 284.8 eV. The Fourier transform infrared (FT-IR) measurements were carried out on a Vertex 70 (Bruker) spectrometer and a gold integrating sphere (A562, Bruker) in KBr pellet, scanning from 4000 to 400 cm^{-1} at room temperature. Raman spectroscopy analysis was carried on a Renishaw InVia Qontor Raman spectrometer. Inductively coupled plasma optical emission spectrometry (ICP-OES) was performed on a PerkinElmer 8300.

X-ray absorption fine structure (XAFS) analyses.[4,5] The extended X-ray absorption fine structure (EXAFS) and X-ray absorption near edge structure (XANES) of Pt L_3-edge were performed at the BL11B beamlines at the Shanghai Synchrotron Radiation Facility (SSRF) (Shanghai, China). Before the analysis at the beamline, samples were pressed into thin sheets with 1 cm in diameter and sealed using Kapton tape film. The XAFS spectra were recorded at room temperature using a 4-channel Silicon Drift Detector (SDD) Bruker 5040. Data reduction, data analysis, and EXAFS fitting were performed and analyzed with the Athena and Artemis programs of the Demeter data analysis packages that utilizes the FEFF6 program to fit the EXAFS data. The energy calibration of the sample was conducted through standard Pt foil, which as a reference was simultaneously measured. A linear function was subtracted from the pre-edge region, then the edge jump was normalized using Athena software. The χ(k) data were isolated by subtracting a smooth, third-order polynomial approximating the absorption background of an isolated atom. The k^3-weighted $\chi(k)$ data were Fourier transformed after applying a HanFeng window function ($\Delta k = 1.0$). For EXAFS modeling, the global amplitude EXAFS (*CN, R,* σ^2 and ΔE_0) were obtained by nonlinear fitting, with least-squares refinement, of the EXAFS equation to the Fourier-transformed data in *R*-space, using Artemis software, EXAFS of the Pt foil is fitted and the obtained amplitude reduction factor S_0^2 value (0.797) was set in the EXAFS analysis to determine the coordination numbers (*CNs*) in the Pt-Pd and Pt-Pt scattering path in sample. For Wavelet Transform analysis,[6] the χ(k) exported from Athena was imported into the Hama Fortran code. The parameters were listed as follow: R range: 1–4 Å, k range: 0–

10 $Å^{-1}$, k weight: 3, and Morlet function with κ=15, σ=1 was used as the mother wavelet to provide the overall distribution.

Electrochemical measurements. Hydrogen evolution reaction (HER) measurements were performed with a standard three-electrode system in 0.5 M H_2SO_4 (pH=0), 1.0 M PBS (pH≈7, Mix 1 M K_2HPO_4, 1 M KH_2PO_4 and 1 M NaCl to neutral) and 1.0 M KOH (pH=14) on CHI 660E electrochemical analyzer (CHI Instruments, Shanghai, Chenhua Co., Ltd.) at room temperature in N_2-saturated atmosphere. Glassy carbon electrode (GCE) with diameter of 3 mm coated with catalysts was used as working electrode. The saturated calomel electrode (SCE), Ag/AgCl and Hg/HgO were used as reference electrodes in acidic, neutral and alkaline media, respectively. Graphite rod was used as counter electrode. The reference electrodes of SCE, Ag/AgCl and Hg/HgO were calibrated with respect to a reversible hydrogen electrode (RHE).[7] 3 mg of each prepared sample was mixed with 1 mL of absolute ethyl alcohol and 20 μL of Nafion ethanolic solution (5 wt%) using ultrasonication for 30 min. 5 μL of the sample was dropped cast onto the glassy carbon electrode and the electrode was dried in air for 10 min, then used as the working electrode for the electrochemical measurement. The measured potential corresponding to the SCE Ag/AgCl and Hg/HgO reference electrode was converted and versus the reverse hydrogen electrode (RHE) by using the Nernst equation:

$$E_{vs.RHE} = E_{vs.SCE} + E^0_{SCE}(0.244\ V) + 0.0591 \cdot pH \quad \text{(S1)}$$

$$E_{vs.RHE} = E_{vs.Ag/AgCl} + E^0_{Ag/AgCl}(0.197\ V) + 0.0591 \cdot pH \quad \text{(S2)}$$

$$E_{vs.RHE} = E_{vs.Hg/HgO} + E^0_{Hg/HgO}(0.098\ V) + 0.0591 \cdot pH \quad \text{(S3)}$$

Where $E_{vs.RHE}$ is the potential in RHE scale, $E_{vs.SCE}$, $E_{vs.Ag/AgCl}$ and $E_{vs.Hg/HgO}$ are the measured potential against the SCE reference electrode, E^0_{SCE} = 0.244 V in saturated KCl solution, $E^0_{Ag/AgCl}$ = 0.197 V and $E^0_{Hg/HgO}$ = 0.098 V at 25 °C. The extent of *iR* compensation is 90% at all pH media.[8,9]

Under the same procedure, Pd, $Pd_7@Pt_1$, $Pd_7@Pt_3$, $Pd_7@Pt_5$, Pt and commercial Pt/C (20 wt%) working electrodes were prepared and kept the same loading of all catalysts on GCE. The accelerated durability tests were performed by applying the cyclic voltammetry (CV) potential sweeps between -0.02 V and -0.04 V (reversible hydrogen electrode (RHE)) at scan rate of 100 mV/s for 20 cycles respectively in 0.5 $_M$ H_2SO_4, 1.0 $_M$ PBS and 1.0 $_M$ KOH until the curve overlap stability can be tested, the linear sweep voltammetry (LSV) curve was recorded at a scan rate of 5 mV/s. The current density for the HER measurement was normalized by the geometric surface area of the electrode. Tafel slopes were obtained by fitting the linear region of the overpotential against versus logarithm of current density (log j) plot into the Tafel equation. Electrochemical impedance spectroscopy (EIS) was measured in set frequency range of 10^5-0.05 Hz, and the voltage was the measured at open circuit potential corresponding to 10 mV to obtain the solution resistance (R_S), and all data were corrected with R_S. EIS spectrum was fitted semicircle by the Z-view software. Intensity-time (i-t) curve is used to measure the ability of a catalyst to maintain its original activity for a long time, sample interval is 0.1 sec.

Before electrolysis, the electrolyte in the cathodic compartment was bubbled with Ar gas for 1 h. A steady supply of Ar gas was delivered at a rate of 50.0 sccm. The cathode compartment was vented directly into the sampling loop of a gas chromatograph (GC, Fuli 9790). The GC analysis was set up to split the gas sample into two aliquots. One aliquot passed a thermal conductivity detector (TCD), and the other was routed through flame ionization detector (FID). All potentials were *iR*-corrected. The electrochemically active surface area is determined by Pb UPD experiment. The Faradaic efficiency and partial current of H_2 production (FE_{H_2} and i_{H2}) were calculated from GC chromatogram peak areas where V_{H_2} is volume concentration of H_2 based on the calibration of the GC. The equations are as following.[10,11]

$$i_{H2} = V_{H2} \times Q \times \frac{2FP_0}{RT} \quad \text{(S4)}$$

$$FE_{H_2} = \frac{i_{H2}}{i_{total}} \times 100 \quad \text{(S5)}$$

where i_{total} is measured current, F is Faradaic constant, P_0 is pressure, T is temperature and R is ideal gas constant, 8.314 J mol·K^{-1}.

The electrochemical double layer capacitance (C_{dl}) was evaluated to measure the electrochemical active surface area (ECSA) of the catalysts. C_{dl} is linearly proportional to ECSA and a large value of C_{dl} implies a high ECSA.[12,13] By plotting the anodic and cathodic current densities difference ((j_{anodic}−$j_{cathodic}$)/2) against the scan rate, a linear relationship was fitting and the slope is equal to C_{dl}. C_{dl} measured via CV is linearly proportional to ECSA. A series of CVs were conducted in the potential range from 0.1 V to 0.2 V vs. RHE at various scan rates of 20-200 mV·s^{-1} to collect the capacitance charging and discharging currents.

ECSA for the HER was calculated using the equation of:

$$A_{ECSA} = \frac{C_{dl}}{40\ \mu F \cdot cm^{-2}} \tag{S6}$$

Total active sites N:

$$N = \frac{n}{S} \times A_{ECSA} \tag{S7}$$

where n is the number of atoms on the crystal face, and S is the area of the crystal face.

Following formula is used to calculate the active-site normalized TOF:

$$TOF = \frac{total\ turn\ overs}{total\ active\ sites} \tag{S8}$$

For HER select the overpotential between 30-300 mV (V vs.RHE) The corresponding TOF could be calculated by the following equation:

$$TOF = \frac{j \times A_0}{n_{H_2} \times F \times N} \times N_A \tag{S9}$$

where j represents the absolute current density at a given overpotential in mA·cm^{-2}, A_0 is the test geometric area of the working electrode, n_{H_2} is the electron transfer

number per H_2 molecule formed, F is the Faraday constant (96485 C·mol^{-1}), N_A stands for Avogadro constant (6.022×10^{23}).

Computational methods. We employed the Vienna *ab initio* simulation package based on plane waves for conducting density functional theory (DFT) calculations.[14] To describe the adsorbate adsorption on surfaces, we utilized the Perdew–Burke–Ernzerhof (PBE) functional with generalized gradient approximation (GGA) to account for electron exchange-correlation.[15] Here, we account for the van der Waals (VdW) interaction using the Grimm method (DFT-D3).[16] We employed a plane-wave approach with a cutoff energy of 450 eV. The force and energy convergencies within 10^{-5} eV and 10^{-2} eV Å^{-1} were qualified to calculate the system. The calculations for hydrogen binding energy were carried out using a 4 × 4 surface unit cell for all models. The choice of the k-point mesh was thoroughly examined, and ultimately, a 3 × 3 × 1 mesh was selected to adequately sample the Brillouin zone for all computations. For the pristine Pd(111) and Pt(111) surfaces, the metal surfaces were represented using five-layer slabs of Pd(111) and Pt(111). The lower two layers were held at the optimized bulk lattice constant, while the upper two layers were permitted to undergo relaxation. Furthermore, in the case of other Pd_x@Pt_y models, the lower layers were held fixed, while the upper two layers were allowed to undergo relaxation. A separation of 15 Å was employed along the Z direction to avoid periodic interactions. The entropies and zero-point energies of surface species were determined by calculating their vibrational frequencies through DFT and applying the harmonic oscillator approximation. The catalytic activity for HER could be evaluated by the hydrogen adsorption free energy of $\Delta G_{H\text{-}ads}$ which proposed by Noskov.[17] The $\Delta E_{H\text{-}ads}$ is the hydrogen adsorption energy:

$$\Delta E_{H-ads} = E_{H-ads} - E_{cat} - 0.5\Delta E_{H_2} \quad \text{(S10)}$$

Here, $E_{H\text{-}ads}$ represents the total energy of the catalyst with a hydrogen atom, while E_{cat} corresponds to the total energy of the catalyst without the hydrogen atom. The term E_{H2} denotes the total energy of the hydrogen molecule.

The Gibbs free energy (ΔG_{H^*}) associated with hydrogen adsorption can be calculated using the following equation:

$$\Delta G_{H^*} = \Delta E_{ads} + \Delta E_{ZPE} - T\Delta S + \int C_p dT + \Delta G_{pH} \quad \text{(S11)}$$

where ΔE_{ZPE}, $T\Delta S$, and $\int C_p dT$ referred to the change in zero-point energies, the change in entropy at temperature T, and the enthalpic temperature correction. We corrected by the vibrational frequency calculations at 298.15 K. ΔG_{pH} represents the change in the pH of solution and the difference in electrode potential. The ΔG_{pH} can be calculated by following equations.

$$\Delta G_{pH} = 2.303 k_b T pH \quad \text{(S12)}$$

where k_b and pH are the Boltzmann constant, and pH of the solution, respectively. In our calculation, we assumed that the HER reaction is employed under highly acidic conditions, where pH = 0, thus, $\Delta G_{pH} = 0$.

Supporting Figures

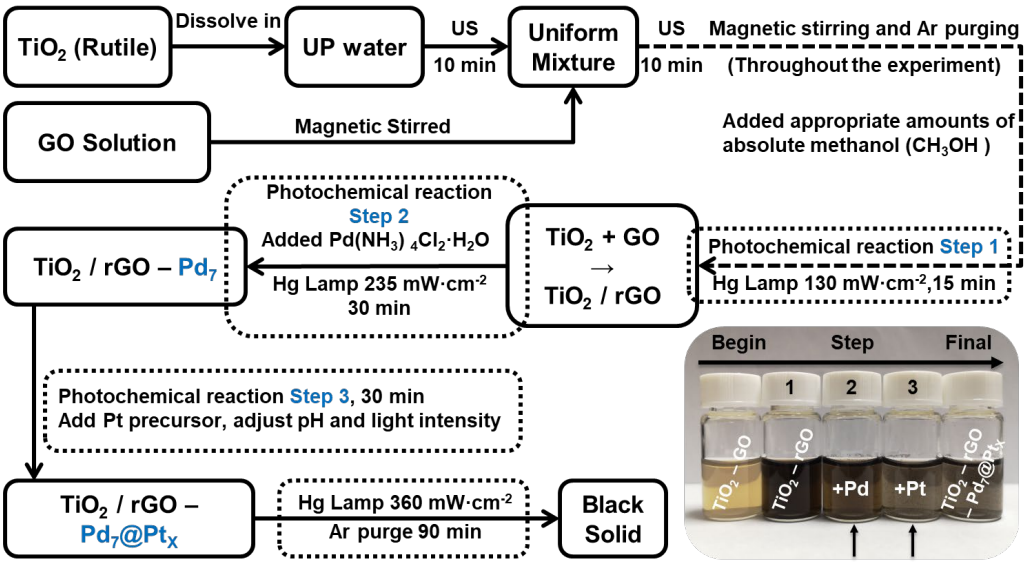

Fig. S1 Preparation procedure and the corresponding optical image (insert) of solutions in different preparation steps of TiO_2-rGO-Pd@Pt core-shell structures.

Note: $Pd_7@Pt_x$ core-shell HNCs synthesis was achieved through a photo-driven seed-mediated growth approach utilizing preformed Pd tetrahedrons as physical templates for photodeposition of various Pt amounts onto their surface, which mainly involved a three-step process. In step 1, GO was uniformly mixed with TiO_2 in a desired mass ratio and photochemically reduced to rGO to improve the conductivity of photoelectrons. The amount of oxygen functional groups decreased during this process indicated by the changing of color from light brown to brownish black. In the step 2, the Pd tetrahedral seeds were obtained on the rGO support by photoelectrons generated from TiO_2. In step 3, based on the decreasing order of work functions (Φ) of TiO_2 (Rutile) (-4.13 eV), rGO (-4.68 eV), Pd (-5.60 eV), and Pt (-5.93 eV),[18,19] photogenerated electrons were excited by TiO_2 and subsequently transferred to the Pd tetrahedral seeds through rGO, triggering the growth of Pt shell.

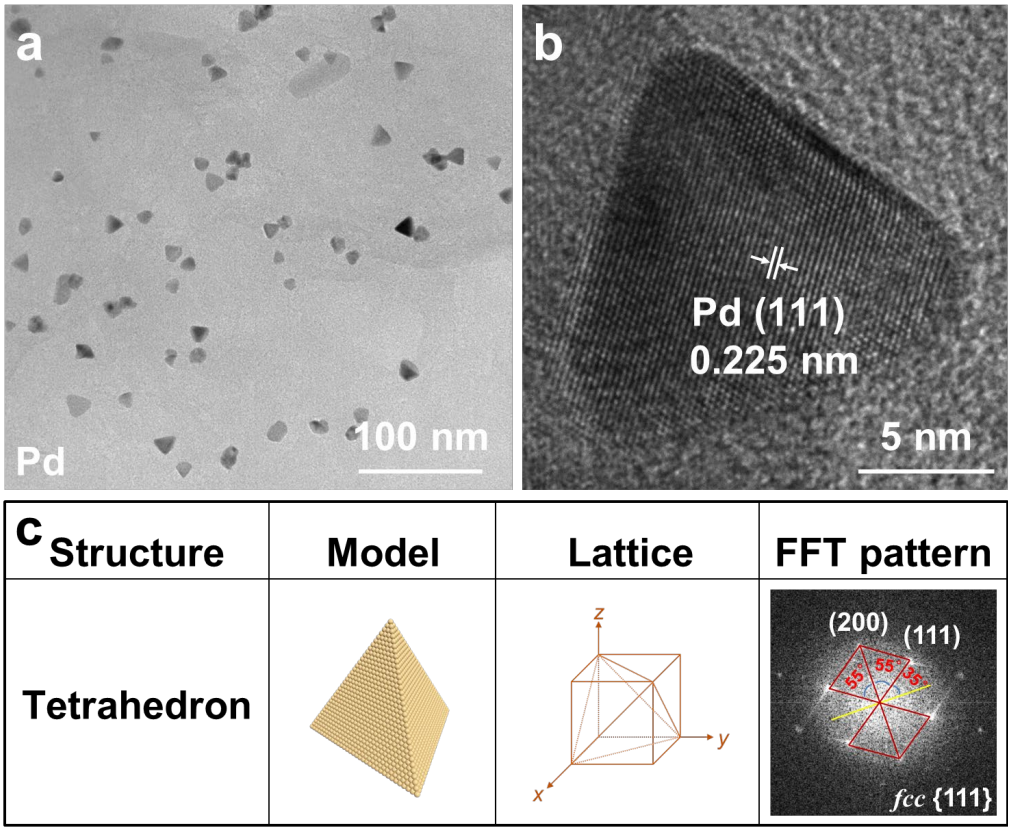

Fig. S2 (a) TEM and (b) HRTEM of Pd tetrahedron (c) Corresponding crystal structure analysis.

Note: Based on our previous work, graphene is demonstrated to facilitate electron transfer, which not only contributes to reducing the rate of Pd nucleation and growth but also provides a stable surface for the controlled growth of metal nanocrystals. Pd tetrahedral nanocrystals can form a stable configuration on rGO.

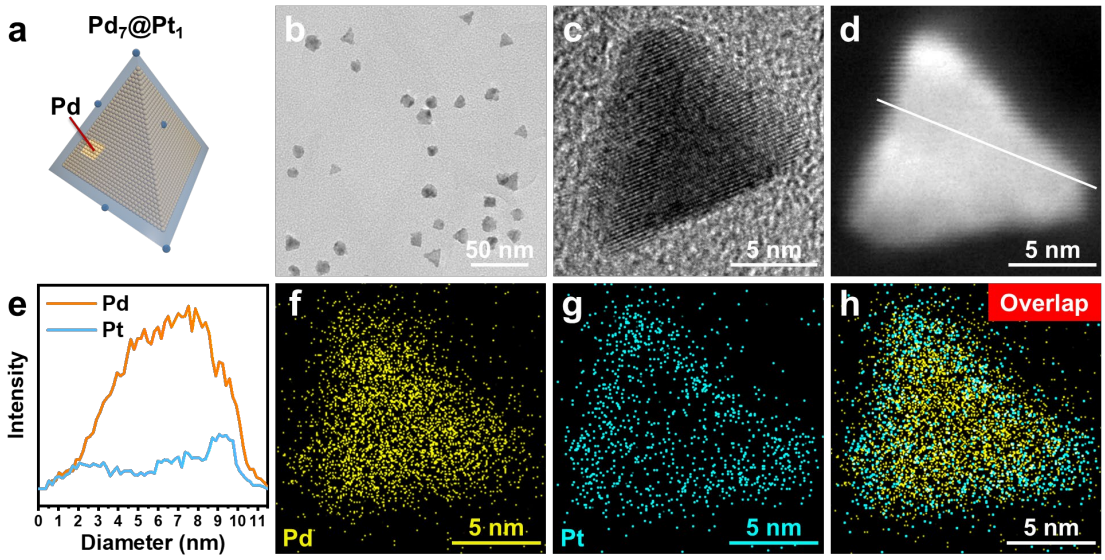

Fig. S3 (a) Schematic model, (b) TEM and (c) HRTEM images of $Pd_7@Pt_1$. (d) HAADF-STEM image, (e) EDS elemental line scan along the white line in (d) and the corresponding EDS elemental mapping images of (f) Pd, (g) Pt, and (h) Pd, Pt overlap of an individual $Pd_7@Pt_1$ nanoparticle.

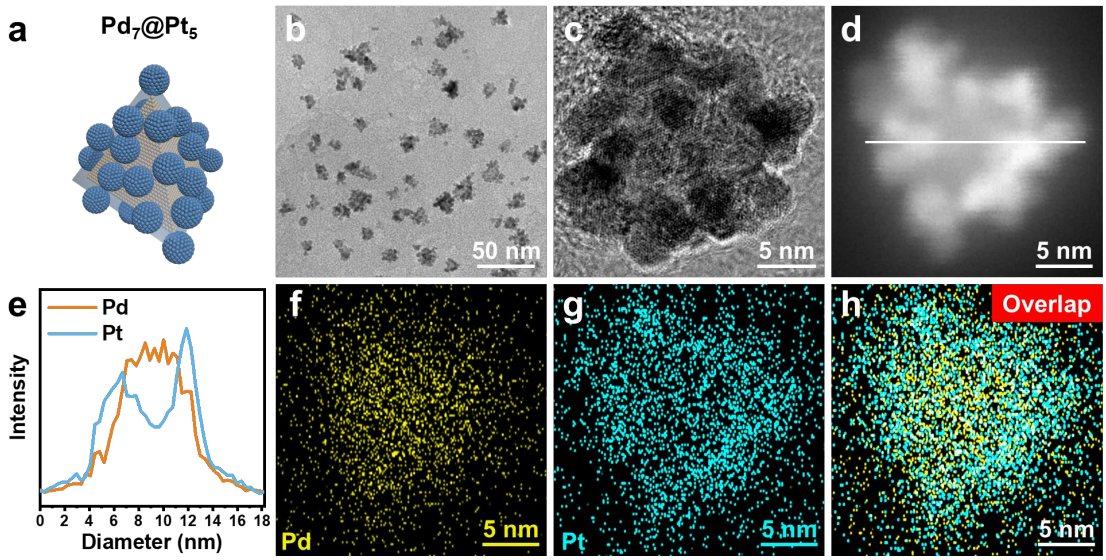

Fig. S4 (a) Schematic model, (b) TEM and (c) HRTEM images of $Pd_7@Pt_5$. (d) HAADF-STEM image, (e) EDS elemental line scan along the white line in (d) and the corresponding EDS elemental mapping images of (f) Pd, (g) Pt, and (h) Pd, Pt overlap of an individual $Pd_7@Pt_5$ nanoparticle.

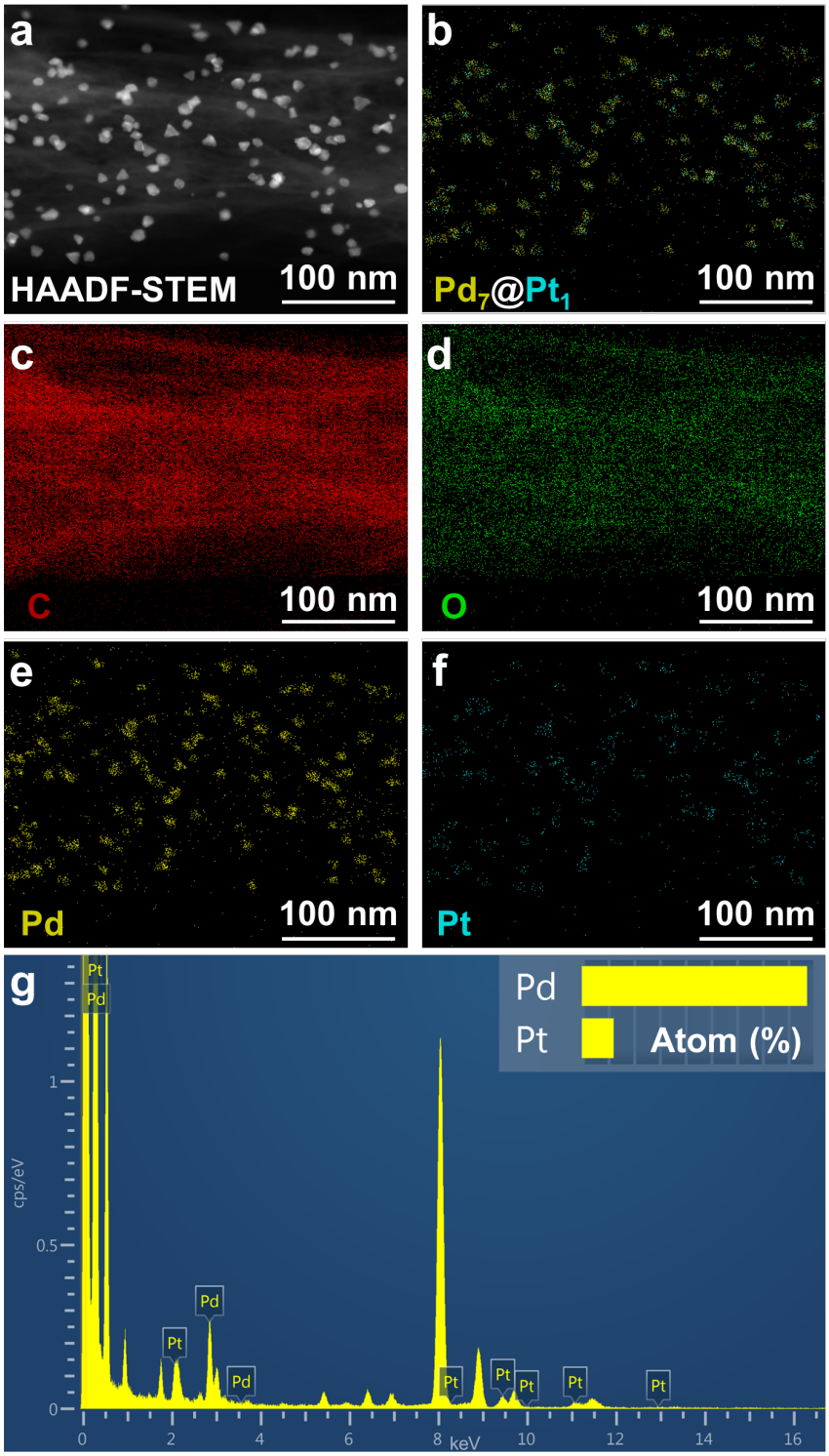

Fig. S5 Low magnification (a) HAADF-STEM image and the corresponding EDS elemental mapping images of (b) Pd, Pt overlap, (c) C, (d) O, (e) Pd, (f) Pt, and (g) atomic ratio EDS spectrum of $Pd_7@Pt_1$.

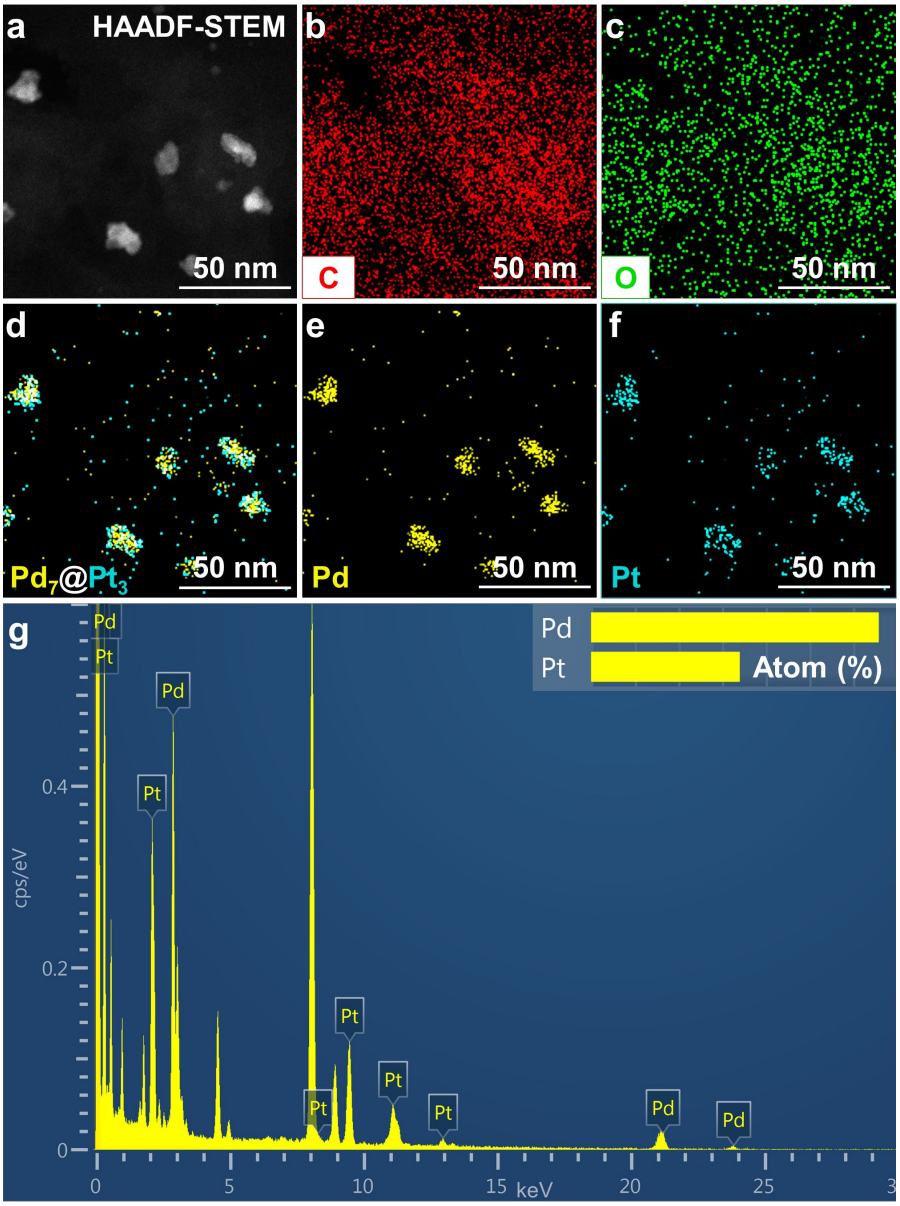

Fig. S6 Low magnification (a) HAADF-STEM image and the corresponding EDS elemental mapping images of (b) C, (c) O, (d) Pd, Pt overlap, (e) Pd, (f) Pt, and (g) atomic ratio EDS spectrum of $Pd_7@Pt_3$.

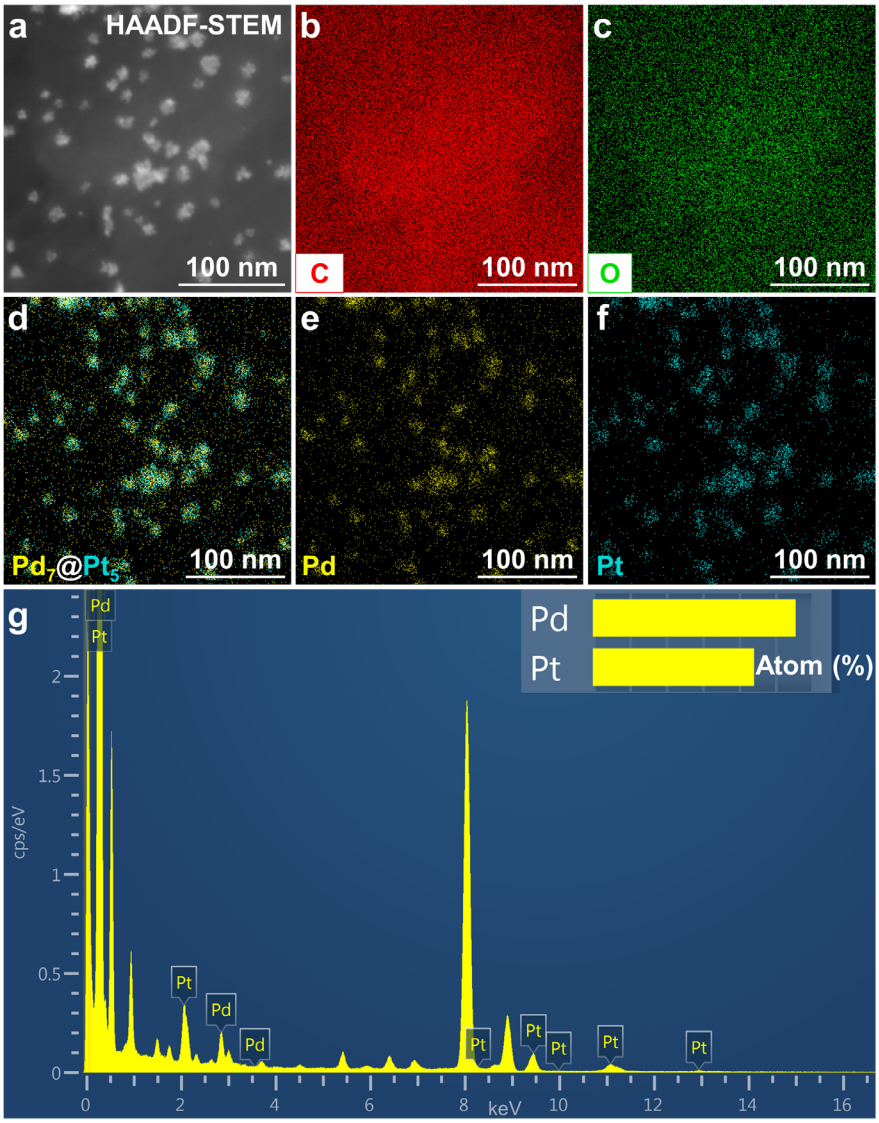

Fig. S7 Low magnification (a) HAADF-STEM image and corresponding EDS elemental mapping images of (b) C, (c) O, (d) Pd, Pt overlap, (e) Pd, (f) Pt, and (g) atomic ratio EDS spectrum of $Pd_7@Pt_5$.

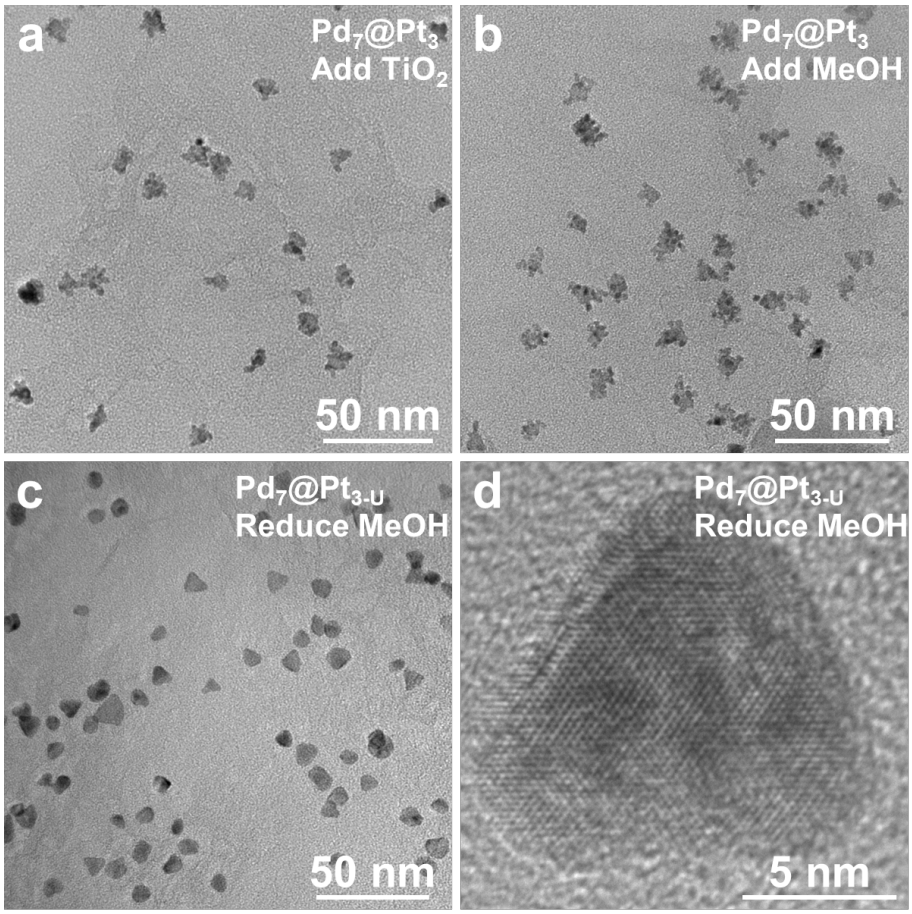

Fig. S8 TEM images of $Pd_7@Pt_3$ HNCs with (a) the addition of TiO_2 and (b) the addition of MeOH. (c) TEM and (d) HRTEM images of $Pd_7@Pt_{3\text{-}U}$ HNCs.

Note: The addition of methanol changed the apparent rate of photoelectrons[20].

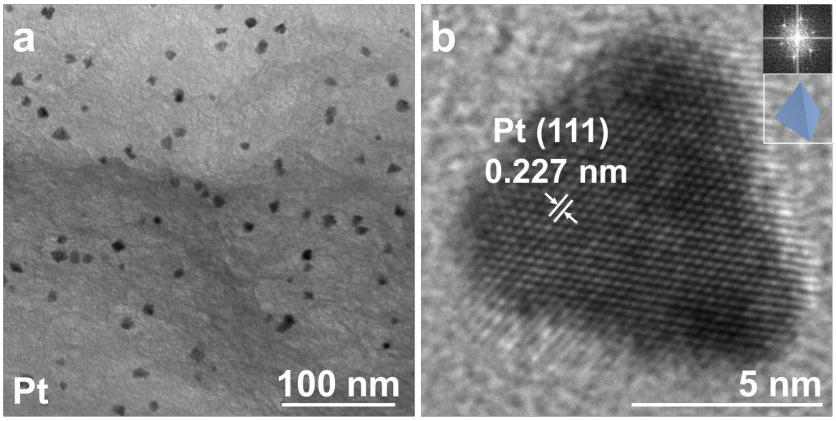

Fig. S9 (a) TEM and (b) HRTEM of Pt_{10} (The insets in b) are the corresponding FFT pattern and simulation diagram, respectively).

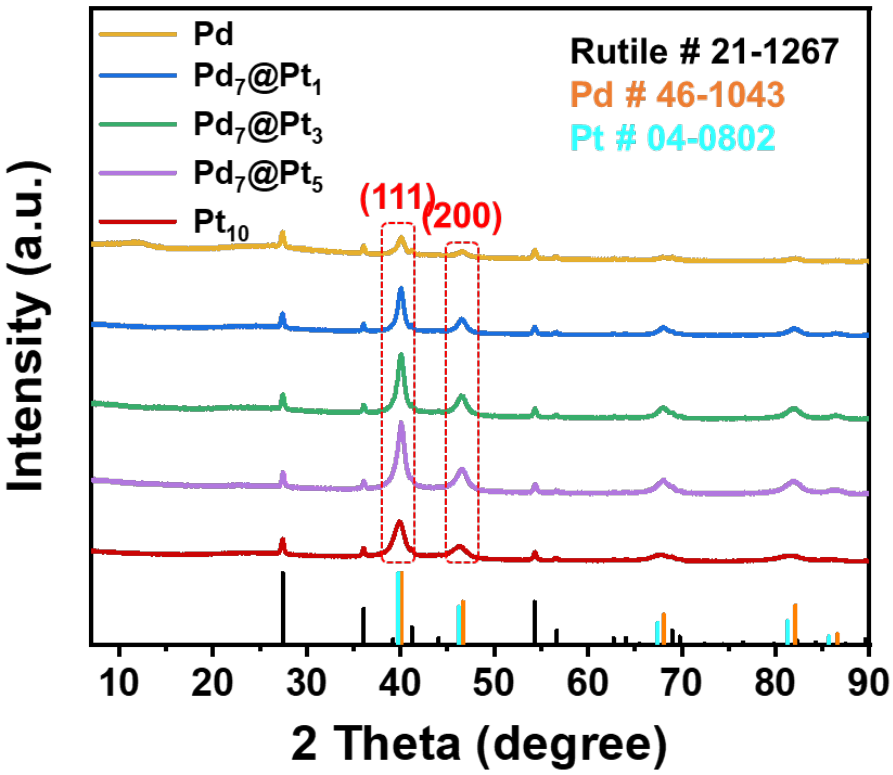

Fig. S10 XRD patterns of supported Pd, $Pd_7@Pt_1$, $Pd_7@Pt_3$, $Pd_7@Pt_5$ and Pt_{10}.

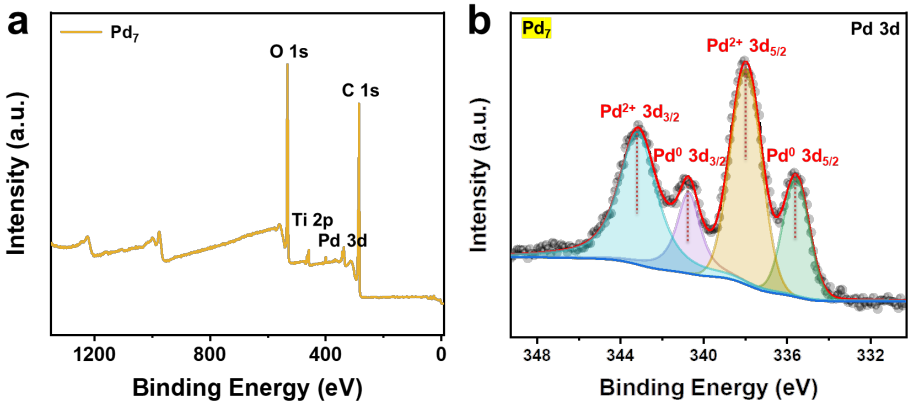

Fig. S11 (a) XPS survey and (b) Pd 3d core-level XPS spectra of Pd_7.

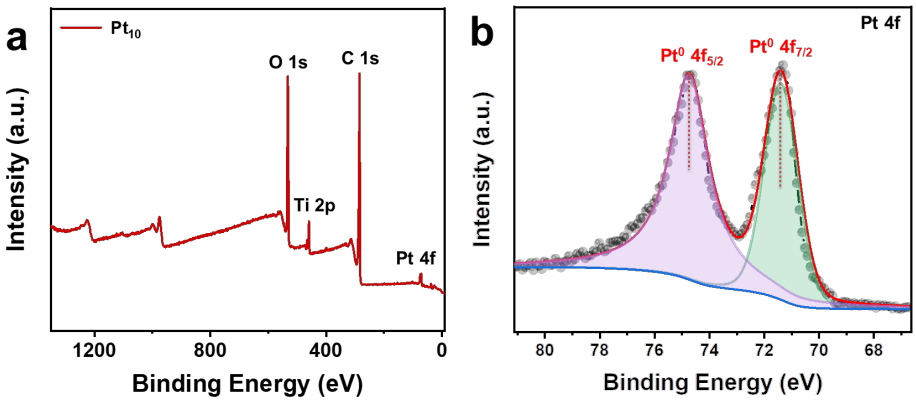

Fig. S12 (a) XPS survey and (b) Pt 4f core-level XPS spectra of Pt_{10}.

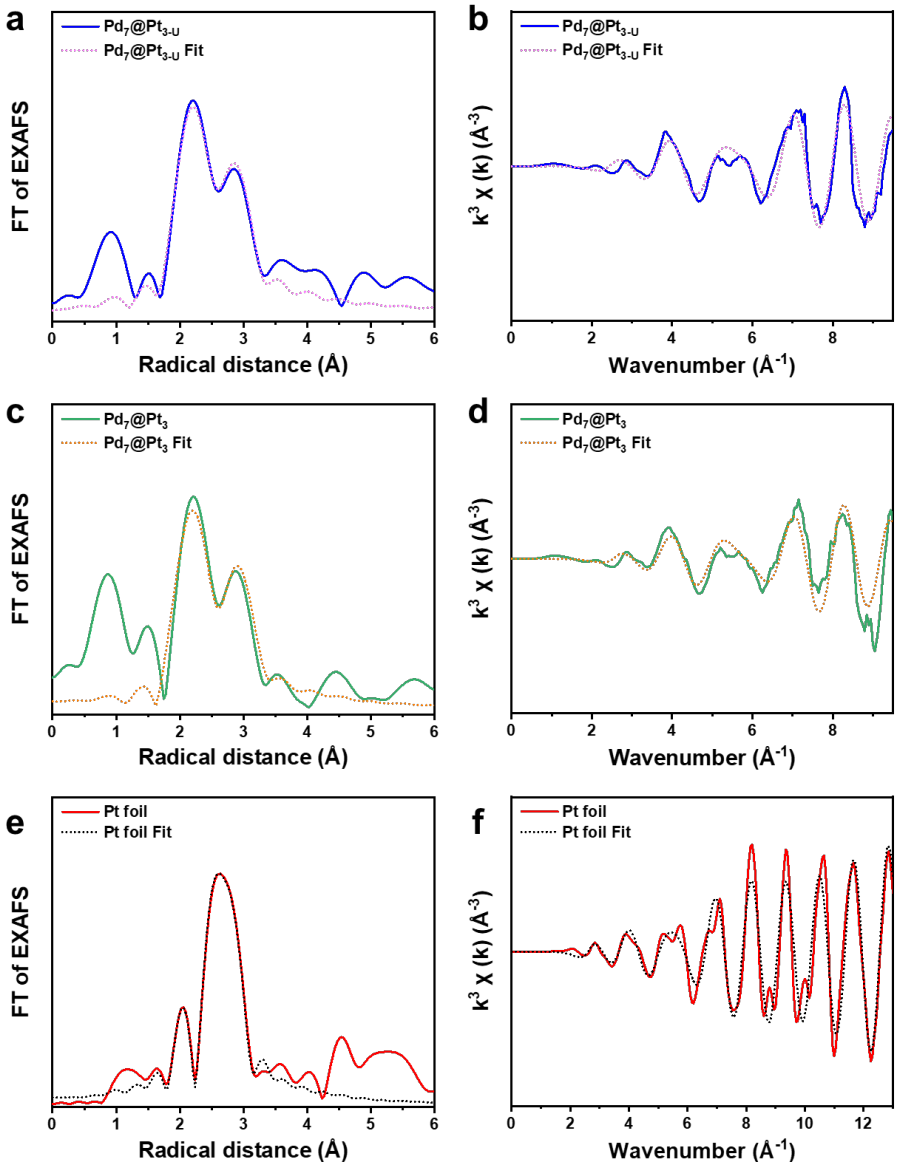

Fig. S13 The raw data (solid curves) and corresponding fitting curves (dashed curves) of Pt L_3-edge EXAFS spectra of (a, b) $Pd_7@Pt_{3\text{-}U}$, (c, d) $Pd_7@Pt_3$ and (e, f) Pt foil in *R* space and *k* space.

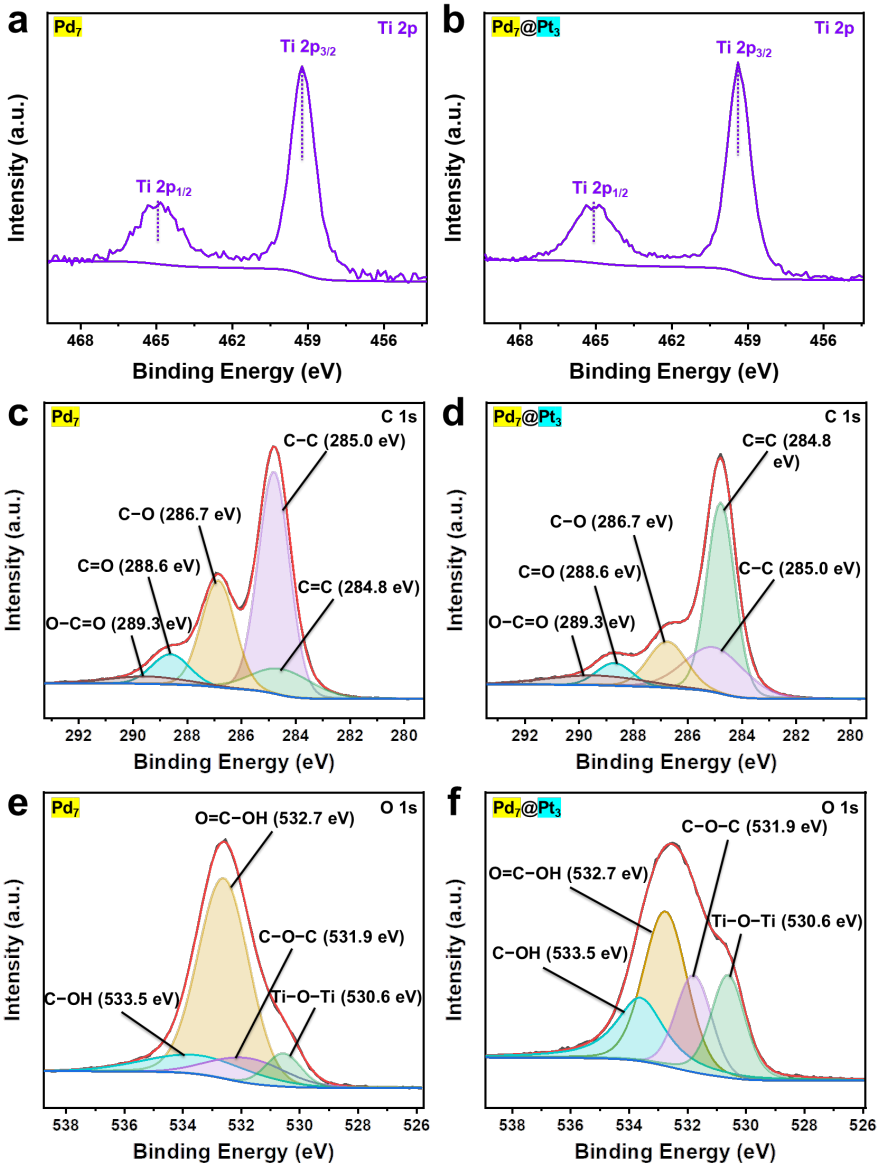

Fig. S14 Ti 2p XPS spectra of (a) Pd_7 and (b) $Pd_7@Pt_3$, C 1s XPS spectra of (c) Pd_7 and (d) $Pd_7@Pt_3$, O 1s of (e) Pd_7 and (f) $Pd_7@Pt_3$.

Note: The core level C 1s spectra can display five peaks with binding energies at 289.3 eV, 288.6 eV, 286.7 eV, 285.0 eV and 284.8 eV are assigned to O−C=O and C=O (carboxyl), C−O (hydroxyl and epoxide), C−C (sp^3 carbon skeleton) and C=C (sp^2 carbon skeleton), respectively,[21] and the intensities of the peaks associated with oxygen species could be divided into four peaks for C−OH (533.5 eV), O=C−O (532.7 eV), C–O–C (531.9 eV) and Ti−O−Ti bond (530.6 eV) [22] according to the high-resolution spectra of O 1s.

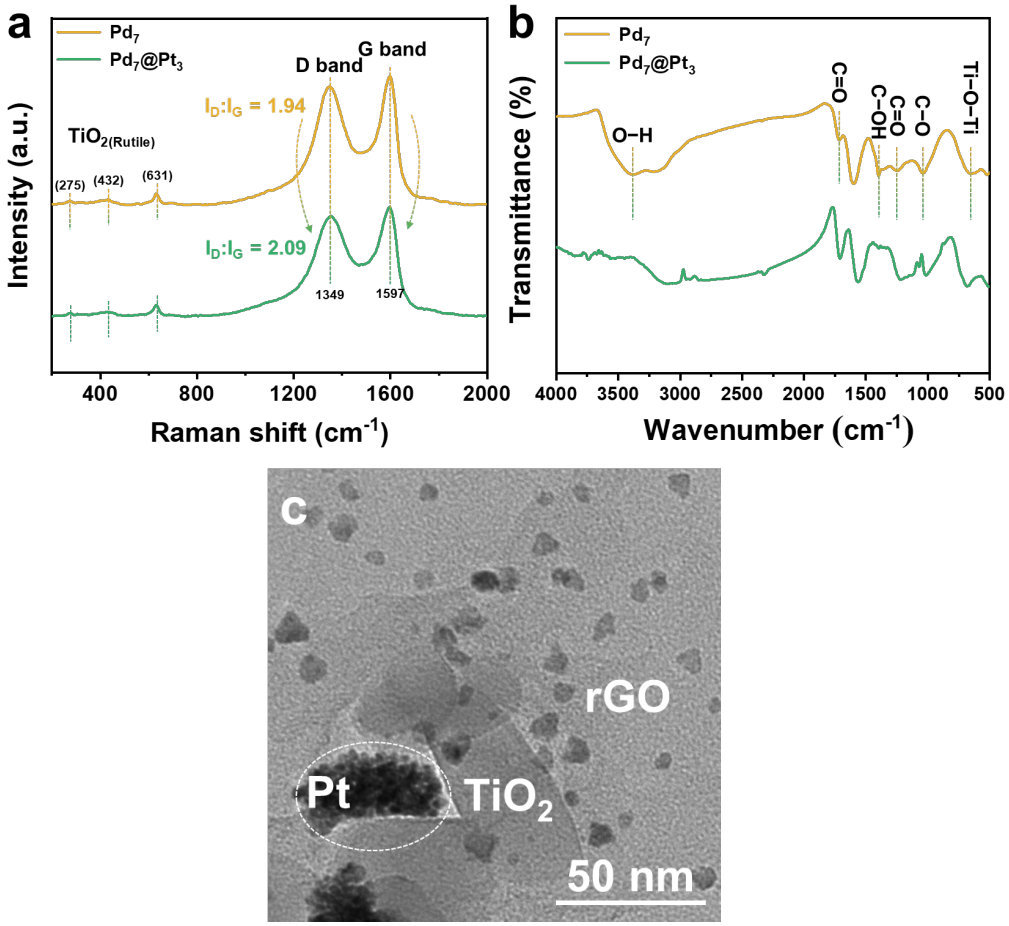

Fig. S15 (a) Raman and (b) FT-IR spectra of Pd_7 and $Pd_7@Pt_3$. TEM of Pt deposition site in $Pd_7@Pt_3$ (c) when rGO reduction degree is same as Pd_7.

Note: Compared with the Raman spectrum of Pd_7, the peak intensity of $Pd_7@Pt_3$ decreases overall, indicating that the rGO slice diameter size is reduced and the layers are peeled off,[23] which facilitates photogenerated electrons transfer on the rGO to form the $Pd_7@Pt_3$ core-shell HNCs. The reduction of rGO can be further demonstrated through Fourier transform infrared spectroscopy (FT-IR) analysis. The characteristic D band at 1349 cm^{-1} representing the edge planes and structural defects and G band at 1597 cm^{-1} ascribe the in-plane stretching vibration of carbon atom sp^2 hybridization.[24] Due to the decrease of oxide functional groups from rGO during the formation of $Pd_7@Pt_3$ core-shell structure, the intensity ratio of D to G band (I_D/I_G) rises from 1.94 to 2.09, reflecting the indication of the disorder degree in graphene layer and the reduction of graphitization degree during the illumination.[25] The attenuation of absorption peaks of O−H (hydroxyl groups) stretching vibrations (3383 cm^{-1}), C=O (carboxylates/ketones and epoxy functional groups, respectively) stretching vibrations (1721 cm^{-1} and 1248 cm^{-1}, respectively) and C−O stretching vibrations (1052 cm^{-1}) indicate the decrease of oxygen functional groups. Meanwhile, due to the recuperation of the aromatic structure, the absorption bands associated with the C=C bond at 1601 cm^{-1} become sharper.[26]

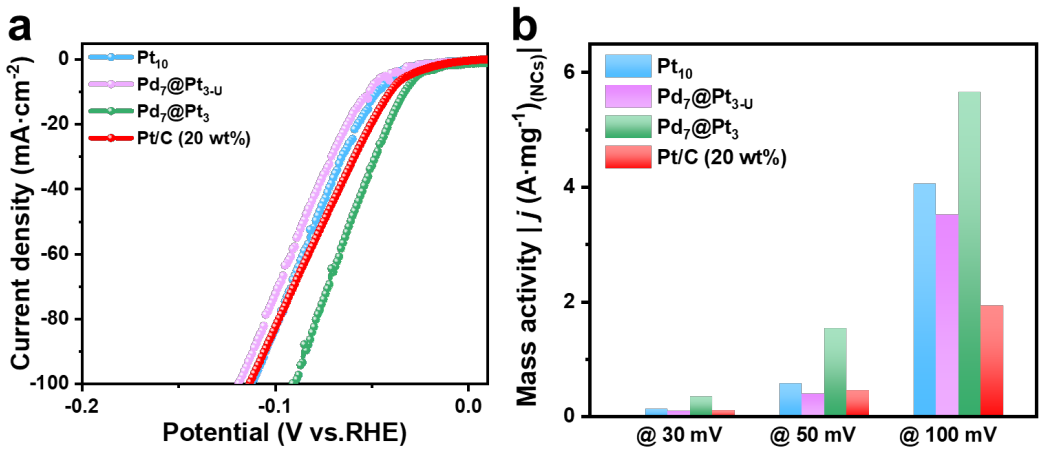

Fig. S16 Comparison of HER performance in 0.5 $_{M}$ H_2SO_4. (a) LSV polarization curves and (b) comparison of normalized current density per mass at different potentials.

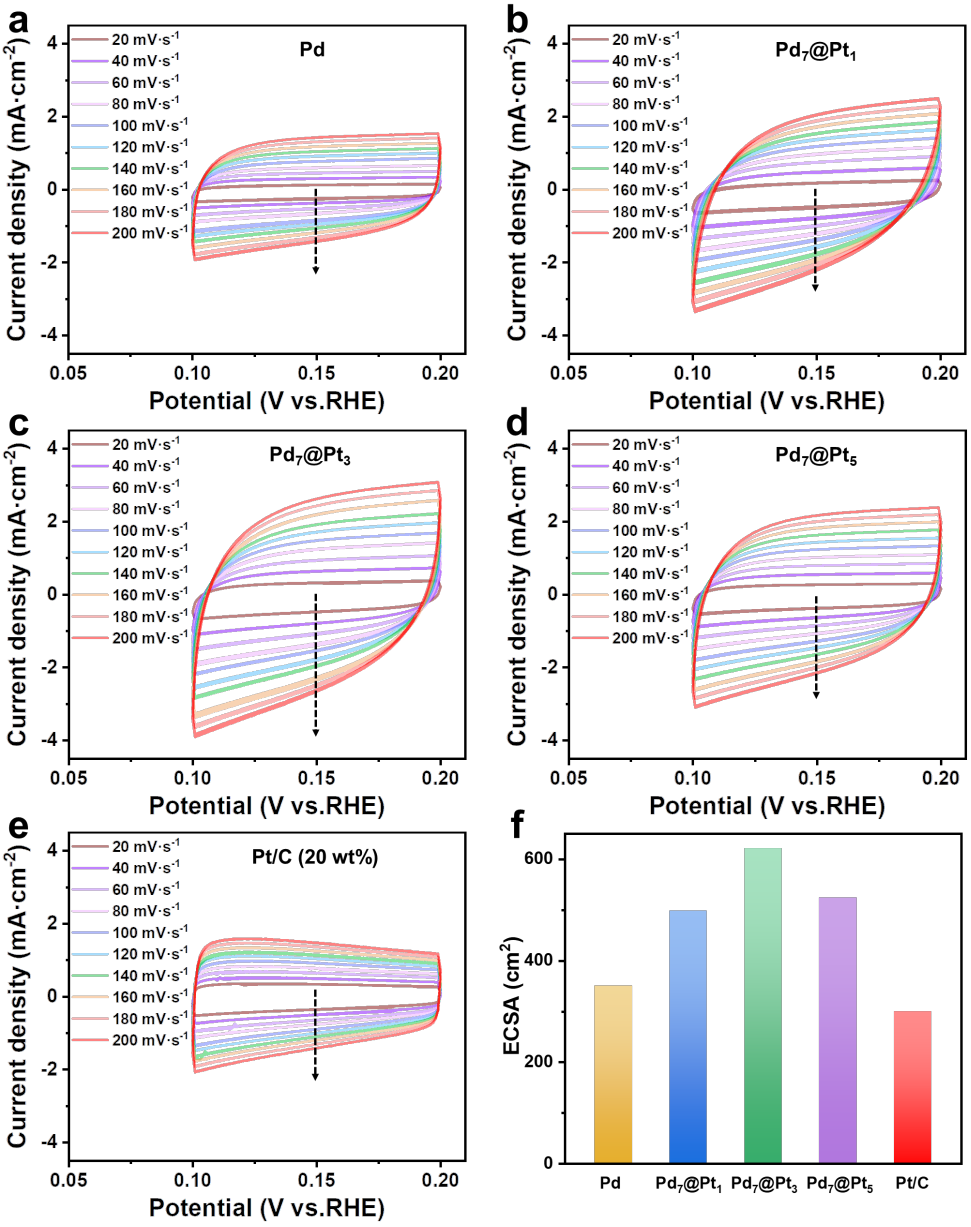

Fig. S17 Cyclic voltammetry curves at different scan rates in the potential range of (a) Pd, (b) $Pd_7@Pt_1$, (c) $Pd_7@Pt_3$, (d) $Pd_7@Pt_5$ and (e) Pt/C (20 wt%) at non-faradaic processes and corresponding (f) ECSA.

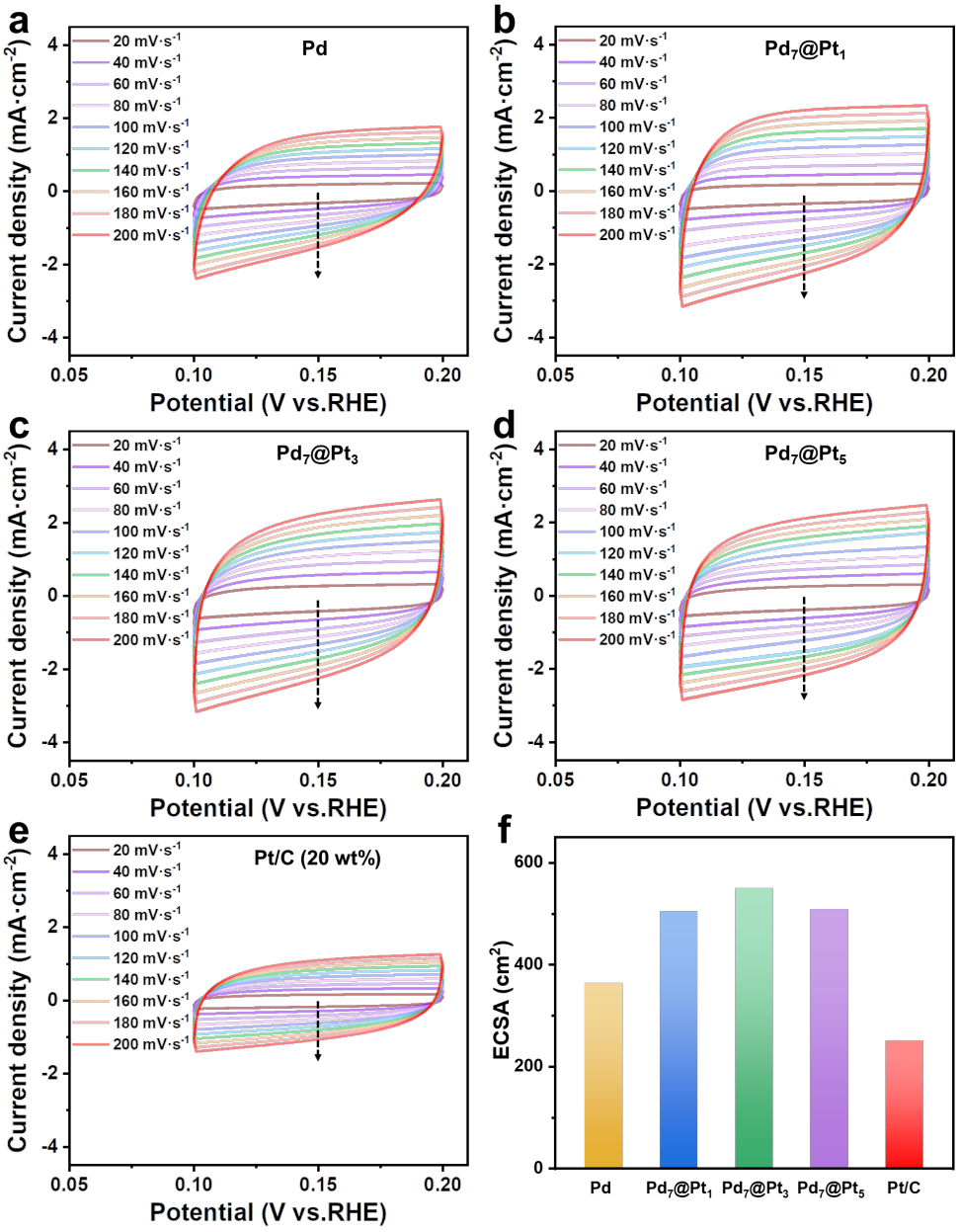

Fig. S18 Cyclic voltammetry curves at different scan rates in the potential range of (a) Pd, (b) $Pd_7@Pt_1$, (c) $Pd_7@Pt_3$, (d) $Pd_7@Pt_5$ and (e) Pt/C (20 wt%) at non-faradaic processes and corresponding (f) ECSA.

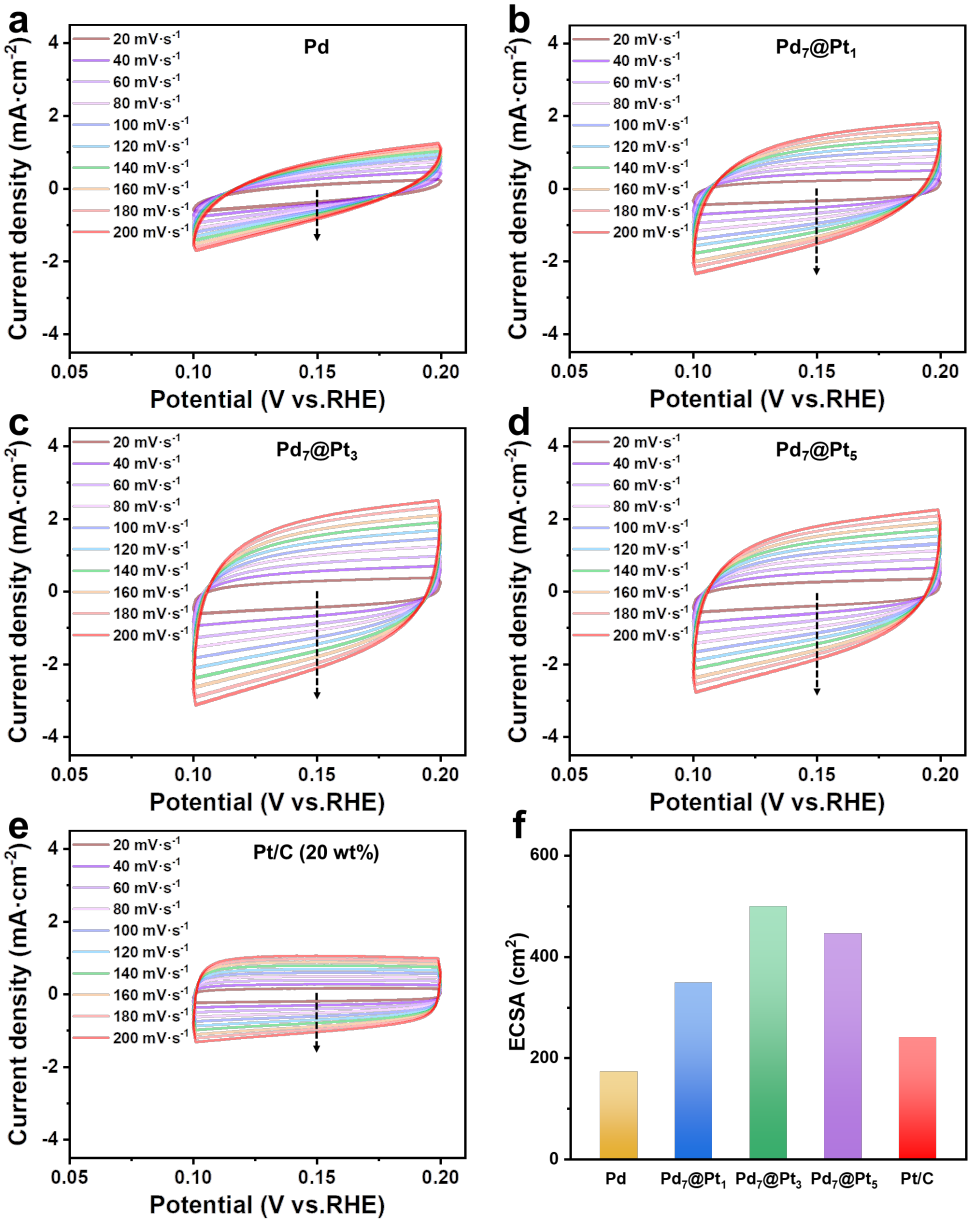

Fig. S19 Cyclic voltammetry curves at different scan rates in the potential range of (a) Pd, (b) $Pd_7@Pt_1$, (c) $Pd_7@Pt_3$, (d) $Pd_7@Pt_5$ and (e) Pt/C (20 wt%) at non-faradaic processes and corresponding (f) ECSA.

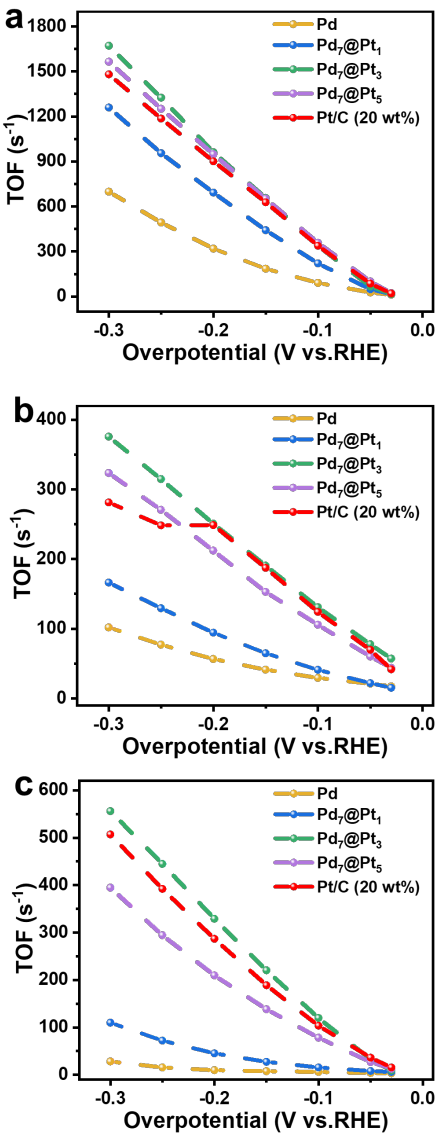

Fig. S20 TOF derived from the ECSAs of Pd, $Pd_7@Pt_x$ and commercial Pt/C (20 wt% Pt) in (a) 0.5 M H_2SO_4, (b) 1.0 M PBS and (c) 1.0 M KOH electrolyte, respectively.

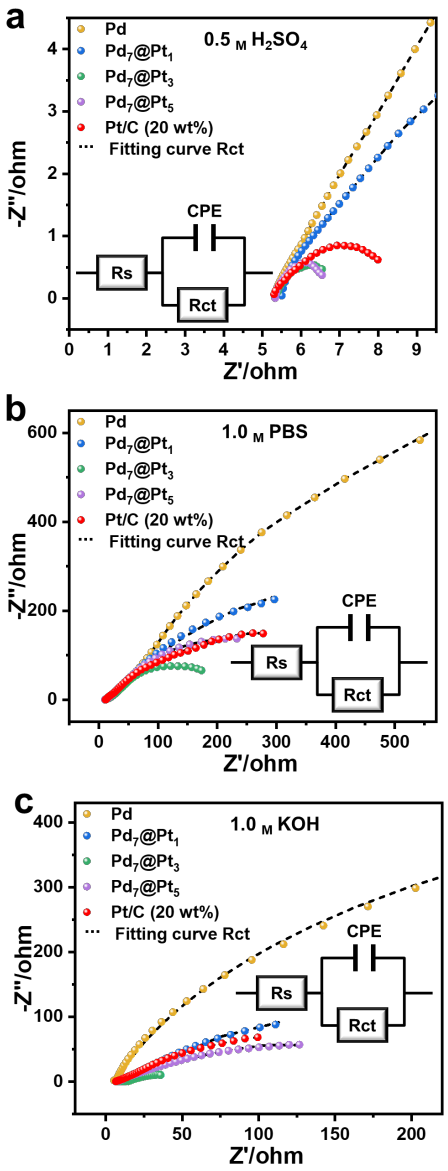

Fig. S21 The Nyquist EIS plots and equivalent circuit diagram of catalysts in (a) 0.5 M H_2SO_4, (b) 1.0 M PBS and (c) 1.0 M KOH.

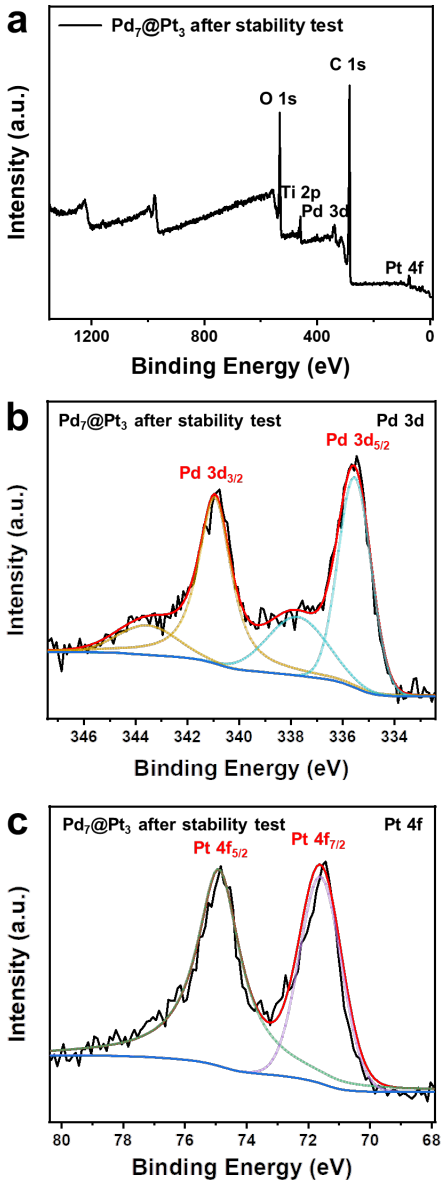

Fig. S22 (a) XPS survey spectra of $Pd_7@Pt_3$ after stability test. (b) Pd 3d core-level and (c) Pt 4f core-level XPS spectrum of $Pd_7@Pt_3$ after stability test.

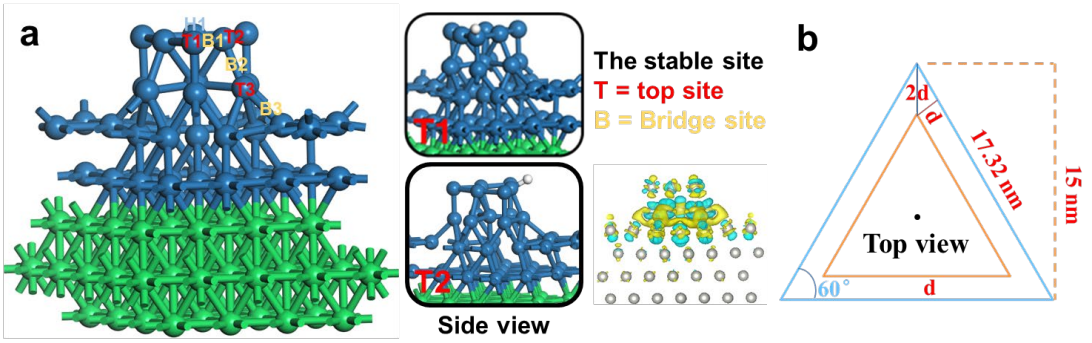

Fig. S23 (a) The model of the layer-island ($Pd_7@Pt_3$) growth model showing the possible adsorption sites. (b) Theoretical simulation diagram of $Pd_7@Pt_{3\text{-}U}$

Note: The lattice spacing between Pd (0.225 nm) and Pt (0.227 nm) is small, so the ideal microscopic density is assumed to be the same. Mass ratio (Pd ∶ Pt) = (7 ∶ 3) → Volume ratio (30 ∶ 7); $Pd_7@Pt_{3\text{-}U}$ mean size ≈ 15 nm; The calculation formula of regular tetrahedron volume is V=⅓ (Floor space × h); $V_{Pd}:V_{Pt} = 30:7 = S_{Pd}\cdot h_{Pd}:S_{Pt}\cdot h_{Pt}$; Where Floor space is 129.9 nm^2, height (h) is 14.14 nm, therefore, d is about 1.5 nm. Theoretically, the thickness of uniform coating Pt is about: 6~7 Pt layers.

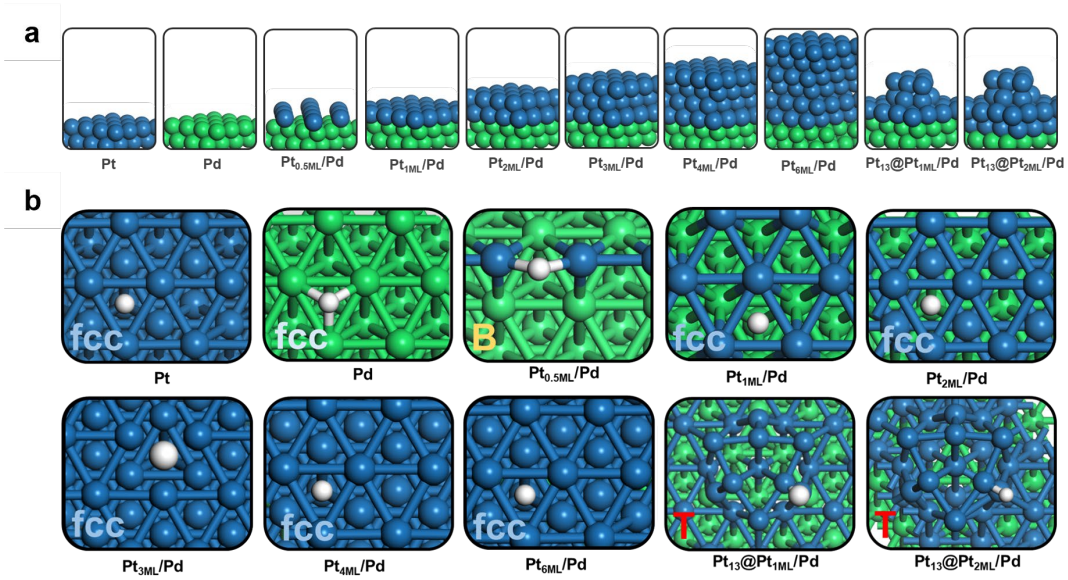

Fig. S24 (a) The DFT optimized structures of all possible models. (b) The most preferable H adsorption site on different surfaces.

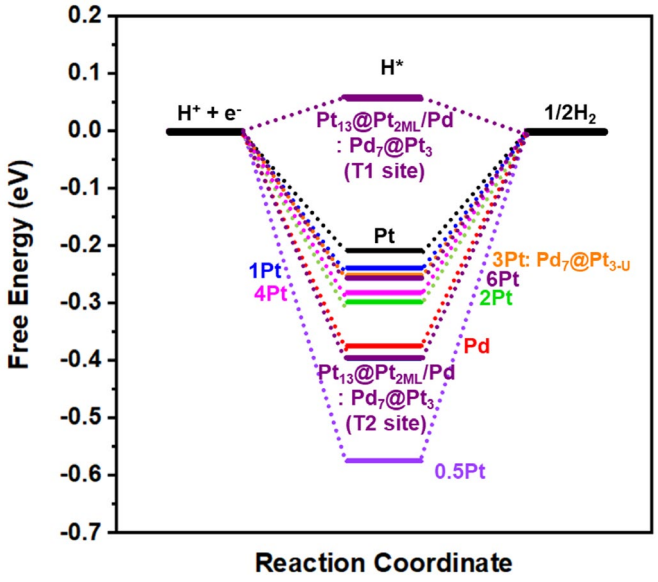

Fig. S25 The calculated free-energy diagram of the HER at the equilibrium potential on all surfaces.

Supporting Tables

Table S1. Abbreviation names of the prepared samples.

Samples	Abbreviation Name
m(TiO_2 : GO)-m(1:15)	TiO_2-GO
Step 1-m(TiO_2 : GO)-m(1:15)	TiO_2-rGO (1)
Step 2-m(TiO_2 : GO)-m(1:15) @7wt% Pd (Tetrahedron)	Pd_7
Step 3-m(TiO_2 : GO)-m(1:15) @7wt% Pd @1wt% Pt(H_2PtCl_6)	$Pd_7@Pt_1$
Step 3-m(TiO_2 : GO)-m(1:15) @7wt% Pd @3wt% Pt(H_2PtCl_6)	$Pd_7@Pt_3$
Step 3-m(TiO_2 : GO)-m(1:15) @7wt% Pd @5wt% Pt(H_2PtCl_6)	$Pd_7@Pt_5$
Step 3-m(TiO_2 : GO)-m(1:15) @7wt% Pd (Tetrahedron)	Pd
Step 3-m(TiO_2 : GO)-m(1:15) @10wt% Pt(H_2PtCl_6)	Pt
Step 3-m(TiO_2 : GO)-m(1:15) @7wt% Pd @3wt% uniform coated Pt)	$Pd_7@Pt_{3\text{-}U}$

Table S2. The comparative Pd/Pt ratio determined by ICP-OES calculations and the analysis of EDS spectrum.

Sample	Total mass m_0 (mg)	Volume V_0 (mL)	Element	Element concentration C_0 (mg/L)	Element content C_x (mg/kg)	Element percentage W (%) of ICP-OES calculations	Analysis of EDS spectrum (Pd：Pt)
$Pd_7@Pt_1$	9.9	25	Pd	2.8005	7004.99	7.00	Pd：Pt ≈ 7：1
			Pt	0.3973	1003.45	1.00	
	9.9	25	Pd	2.7966	6991.49	6.99	
			Pt	0.3991	1007.88	1.01	
$Pd_7@Pt_3$	10.1	25	Pd	2.8046	7013.42	7.01	Pd：Pt ≈ 7：3
			Pt	1.2188	3016.74	3.02	
	10.1	25	Pd	2.8010	7002.88	7.00	
			Pt	1.2124	3001.05	3.00	
$Pd_7@Pt_5$	9.8	25	Pt	2.7925	6983.30	6.98	Pd：Pt ≈ 7：5
			Pt	1.9655	5013.99	5.01	
	9.8	25	Pd	2.8065	7016.31	7.02	
			Pt	1.9609	5002.26	5.00	

Note: The filtrate obtained after the photodeposition reaction was tested by ICE-OES and the results revealed the absence of Pd and Pt, indicating the complete reduction of all precursors. Moreover, the synthesized material was dissolved to determine the content of Pd and Pt, which was found to be in agreement with the theoretical calculation (TiO_2: 2 mg, rGO: 30 mg).

Table S3. Comparison of particle size by XRD calculation and TEM measurement.

	Particle size calculated by TEM (nm)	Particle size measured by XRD (nm)
$Pd_7@Pt_1$	14.1 ± 0.9	13.7
$Pd_7@Pt_3$	15.5 ± 0.5	14.6
$Pd_7@Pt_5$	16.3 ± 1.2	15.8

Note: The particle size was calculated according to the Scherrer formula (S13) combined with the Jade software of XRD.

$$D = K\lambda/(\beta\cos\theta) \quad (S13)$$

K is a constant; λ is the X-ray wavelength; β is the half-width of the diffraction peak; θ is the diffraction angle.

Table S4. Relative amount of C1s spectra components calculation.

	Pd_7 (%)	$Pd_7@Pt_3$ (%)
O−C=O	9.3	8.5
C=O	10.5	10.3
C−O	25.3	18.1
C−C	45.7	20.0
C=C	9.2	43.1

Note: Relative amount (%) of each component was calculated via dividing its peak area (A_X) by the total area of all C 1s components (A_{Tot}). The quantitative analysis of C 1s components shows an observable decrease of oxygen functional groups and increase in pure carbon relative amount in spectra of the TiO_2-rGO-$Pd_7@Pt_3$ in comparison with that of TiO_2-GO-Pd_7. Above results confirm co-reduction of rGO and noble metal during the process in the preparation of $Pd_7@Pt_x$.

Table S5. Mass activities normalization comparison at different potentials.

Catalysts	In 0.5 $_M$ H_2SO_4 ($mA \cdot mg^{-1}$)			In 1.0 $_M$ PBS ($mA \cdot mg^{-1}$)			In 1.0 $_M$ KOH ($mA \cdot mg^{-1}$)		
	30 mV	50 mV	100 mV	50 mV	100 mV	150 mV	50 mV	100 mV	350 mV
Pd	171.5	408.1	1346.8	306.8	425.9	596.5	56.6	87.5	739.1
$Pd_7@Pt_1$	261.3	838.0	3862.6	385.2	722.1	1140.3	135.5	271.7	2820.8
$Pd_7@Pt_3$	345.3	1539.6	5655.0	965.4	1751.0	2619.3	518.0	1837.9	10367.6
$Pd_7@Pt_5$	171.8	780.4	3966.9	536.9	10 60.1	1647.5	314.0	919.4	5969.2
Pt/C (20 wt%)	108.8	454.4	1939.5	303.8	540.6	859.1	157.9	450.5	2709.7

Table S6. Comparison of HER performance of the recent reported Pt-based catalysts in 0.5 M H_2SO_4 electrolyte.

Catalysts	Effective load ($mg \cdot cm^{-2}$)	Overpotential at 10 $mA \cdot cm^{-2}$ (mV)	Tafel slope ($mV \cdot dec^{-1}$)	TOF ($H_2 \cdot s^{-1}$)	References
3D 3h-Pt@Nb_2CT_x	0.1	33.3	29	-	[27] *Adv. Sci.* **2021**, 8, 2102207.
Pt/NBF-ReS_2/Mo_2CT_x	0.1	29	24	-	[28] *Energy Storage Mater.* **2021**, 42, 418-429.
Pt_{SA}/α-MoC_{1-x}@C	0.36	12	27	15.3@50 mV	[29] *Adv. Funct. Mater.* **2022**, 33, 2108464.
PtCoMo@NC	0.56	26	25	-	[30] *Nanoscale* **2020**, 12, 19804-19813.
Au-Pd-Pt aerogels	0.35	33	35	-	[31] *Adv. Energy Mater.* **2020**, 10, 1903857.
PtRu/CC_{1500}	0.016	8	25	13.4@50 mV	[32] *J. Mater. Chem. A* **2020**, 8, 2090-2098.
Bm-5d-Pt	0.49	30	20	51.2@150 mV	[33] *Adv. Funct. Mater.* **2021**, 31, 2105372.
PdP_2@CB	0.285	27.5	29.5	0.32@27.5 mV	[34] *Angew. Chem. Int. Ed.* **2018**, 57, 14862-14867.
CS-PdPt	0.255	26	33	-	[35] *Int. J. Hydrog. Energy* **2020**, 45, 11127-11137.
Pt@NOMC-A	0.5	7	43	-	[36] *J. Colloid Interface Sci.* **2018**, 530, 595-602.
Pt/C/NF	2.9	52	104	-	[7] *Adv. Mater.* **2022**, 34, 2107548.
CDs/Pt-PANI-4	Pt 0.008	30	64.5	-	[37] *Appl. Catal. B Environ.* **2019**, 257, 117905.
PtRu/mCNTs	0.386	28	22.6	-	[38] *Energy Environ. Sci.* **2022**, 15, 102-108.
Pt/B_4C	0.08	31	12.9	-	[39] *J. Mater. Chem. A* **2023**, 11, 4000-4006.
PtN_x/TiO_2	0.015	67	34	38.0@50 mV	[40] *Nano Energy* **2020**, 73, 104739.
PtW_6O_{24}/C	0.92	22	29.8	33.4@100 mV	[41] *Nat. Commun.* **2020**, 11, 490-496.
PtW NPs/C	0.02	19.4	27.8	-	[42] *J. Am. Chem. Soc.* **2020**, 142, 17250-17254.
Pt_1/OLC	0.51	38	36	40.8@100 mV	[43] *Nat. Energy* **2019**, 4, 512-518.
Pd@PtCu/C	0.15	19	26	-	[44] *ACS Energy Lett.* **2018**, 3, 940-945.
Octahedral Pt-Pd SAA	0.15	50	28	-	[45] *ACS Catal.* **2019**, 9, 9350-9358.
$MoPt_2$-$MoNi_4$/Mo_2C	1.6	27	28	-	[46] *Chem. Eng. J.* **2023**, 470, 144375.
Pt cluster/MXene	0.19	34	29	7.9@150 mV	[47] *Adv. Funct. Mater.* **2022**, 32, 2110910.
Pd_7@Pt_3 core-shell HNCs	Pd 0.0147 Pt 0.0063	33	23.1	652.6@150 mV	This Work

Table S7. Comparison of HER performance of the recent reported Pt-based catalysts in 1.0 $_M$ PBS electrolyte.

Catalysts	Effective load ($mg \cdot cm^{-2}$)	Overpotential at 10 $mA \cdot cm^{-2}$ (mV)	Tafel slope ($mV \cdot dec^{-1}$)	TOF ($H_2 \cdot s^{-1}$)	References
3D 3h-Pt@Nb_2CT_x	0.1	124	56	-	[27] *Adv. Sci.* **2021**, 8, 2102207.
Pt/NBF-ReS_2/Mo_2CT_x	0.1	49	39	1.4@150 mV	[28] *Energy Storage Mater.* **2021**, 42, 418-429.
Pt_{SA}/α-MoC_{1-x}@C	0.51	36	31	7.2@50 mV	[29] *Adv. Funct. Mater.* **2022**, 33, 2108464.
PtCoMo@NC	0.56	60	159	-	[30] *Nanoscale,* **2020**, 12, 19804-19813.
Au-Pd-Pt aerogels	0.35	47	46	-	[31] *Adv. Energy Mater.* **2020**, 10, 1903857.
PtRu/CC_{1500}	0.016	25	36	4.6@100 mV	[32] *J. Mater. Chem. A* **2020**, 8, 2090-2098.
Bm-5d-Pt	0.49	98	58	-	[33] *Adv. Funct. Mater.* **2021**, 31, 2105372.
PdP_2@CB	0.285	85	72.3	-	[34] *Angew. Chem. Int. Ed.* **2018**, 57, 14862-14867.
CS-PdPt	0.255	50	107	-	[35] *Int. J. Hydrog. Energy* **2020**, 45, 11127-11137.
Pt@NOMC-A	0.5	66	70	-	[36] *J. Colloid Interface Sci.* **2018**, 530, 595-602.
Pt/C/NF	2.9	39	163	-	[7] *Adv. Mater.* **2022**, 34, 2107548.
CDs/Pt-PANI-4	Pt 0.008	134	458	-	[37] *Appl. Catal. B Environ.* **2019**, 257, 117905.
PtRu/mCNTs	0.386	17	48.7	-	[38] *Energy Environ. Sci.* **2022**, 15, 102-108.
Rh@Pt_{2L}	0.13	19	33.6	14@150 mV	[48] *Adv. Energy Mater.* **2022**, 12, 2201548.
PtSA-NT-NF	1.62	24	30	-	[49] *Angew. Chem. Int. Ed.* **2017**, 56, 13694-13698.
Pt/np-$Co_{0.85}Se$	0.0258	55	35	3.93@100 mV	[50] *Nat. Commun.* **2019**, 10, 1743.
Pt_{SA}-NiO/Ni	0.007	27	32	-	[51] *Nat. Commun.* **2021**, 12, 3783.
PANI@Pt/S-TiN NTs/Ti	0.0208	39	37.7	-	[52] *Small* **2022**, 18, 2205603.
PtNb-Nb_2O_5@CC	0.25	225	56.1	0.03@100 mV	[53] *Appl. Catal. B Environ.* **2022**, 318, 121808.
T-Pt-Co_4N	-	27	28.6	40.7@100 mV	[54] *ACS Nano* **2022**, 16, 18038-18047.
$MoPt_2$-$MoNi_4$/Mo_2C	1.6	19	23	0.605@100 mV	[46] *Chem. Eng. J.* **2023**, 470, 144375.
Pt@CoO_x	0.022	82	52	4.6@300 mV	[55] *Angew. Chem. Int. Ed.* **2022**, 61, e202116057.
Pd_7@Pt_3 core-shell HNCs	Pd 0.0147 Pt 0.0063	18	18	190.7@150 mV	This Work

Table S8. Comparison of HER performance of the recent reported Pt-based catalysts in 1.0 M KOH electrolyte.

Catalysts	Effective load ($mg \cdot cm^{-2}$)	Overpotential at 10 $mA \cdot cm^{-2}$ (mV)	Tafel slope ($mV \cdot dec^{-1}$)	TOF ($H_2 \cdot s^{-1}$)	References
3D 3h-Pt@Nb_2CT_x	0.1	61.5	58	-	[27] *Adv. Sci.* **2021**, 8, 2102207.
Pt/NBF-ReS_2/Mo_2CT_x	0.1	37	36	-	[28] *Energy Storage Mater.* **2021**, 42, 418-429.
Pt_{SA}/α-MoC_{1-x}@C	0.42	21	29	11.6@50 mV	[29] *Adv. Funct. Mater.* **2022**, 33, 2108464.
PtCoMo@NC	0.56	51	74	-	[30] *Nanoscale,* **2020**, 12, 19804-19813.
Au-Pd-Pt aerogels	0.35	39	55	-	[31] *Adv. Energy Mater.* **2020**, 10, 1903857.
PtRu/CC_{1500}	0.016	19	28	13.0@100 mV	[32] *J. Mater. Chem. A* **2020**, 8, 2090-2098.
Bm-5d-Pt	0.49	65	44	-	[33] *Adv. Funct. Mater.* **2021**, 31, 2105372
PdP_2@CB	0.285	35	42.1	-	[34] *Angew. Chem. Int. Ed.* **2018**, 57, 14862-14867.
CS-PdPt	0.255	46	88	-	[35] *Int. J. Hydrog. Energy* **2020**, 45, 11127-11137.
Pt@NOMC-A	0.5	42	52	-	[36] *J. Colloid Interface Sci.* **2018**, 530, 595-602.
Pt/C/NF	2.9	63	82	-	[7] *Adv. Mater.* **2022**, 34, 2107548.
CDs/Pt-PANI-4	Pt 0.008	56	58	-	[37] *Appl. Catal. B Environ.* **2019**, 257, 117905.
PtRu/mCNTs	0.386	15	33.5	-	[38] *Energy Environ. Sci.* **2022**, 15, 102-108.
Pt/B_4C	0.08	18	28.3	-	[39] *J. Mater. Chem. A* **2023**, 11, 4000-4006.
Pd@PtCu/C	0.15	60	43	-	[44] *ACS Energy Lett.* **2018**, 3, 940-945.
Rh@Pt_{2L}	0.13	5	30.5	1.5@20 mV	[48] *Adv. Energy Mater.* **2022**, 12, 2201548.
Pt_{SA}-NiO/Ni	0.007	26	27	5.7@ 50 mV	[51] *Nat. Commun.* **2021**, 12, 3783.
Pt/Nb-Co(OH)	0.283	112	82	2@150 mV	[56] *Small* **2023**, 19, 2207569.
Pt/TiB_xO_y	0.038	210	135	33.2@ 50 mV	[57] *ACS Catal.* **2022**, 12, 5970-5978.
Rh@$Pt_{0.83}$ NBs	0.015	44	54.2	-	[58] *Chem. Eng. J.* **2022**, 429, 132414.
Pd@Pt_{4-5L}	0.075	120	43	-	[59] *J. Am. Chem. Soc.* **2019**, 141, 18256-18263.
Pt-F	0.20	74	58	-	[60] *J. Mater. Chem. A* **2023**, 11, 2452-2459.
Pd_7@Pt_3 core-shell HNCs	Pd 0.0147 Pt 0.0063	49	42.7	220.3@150 mV	This Work

Table S9. The calculated FE% of different electrocatalysts.

Electrocatalysts	FE% (0.5 $_M$ H_2SO_4)	FE% (1.0 $_M$ PBS)	FE% (1.0 $_M$ KOH)
$Pd_7@Pt_1$	99.3±1.3	98.4±1.8	98.7±1.1
$Pd_7@Pt_3$	99.7±0.6	99.5±0.8	99.1±1.0
$Pd_7@Pt_5$	98.3±0.9	98.2±1.4	98.0±0.7
Pt	98.5±1.5	96.4±1.6	97.2±1.2
Commercial Pt/C (20 wt%)	96.5±2.4	94.1±3.5	95.5±2.8

Table S10. The coordination of models (CN) from DFT calculations.

Models	CN	No. atom	No. CN	%CN	%UN
Bulk	12	16	192	100.00	0.00
Pt	9	16	144	75.00	25.00
Pd	9	16	144	75.00	25.00
$Pt_{0.5ML}/Pd$	5	8	40	41.67	58.33
Pt_{1ML}/Pd	9	16	144	75.00	25.00
Pt_{2ML}/Pd	9	16	144	75.00	25.00
Pt_{3ML}/Pd	9	16	144	75.00	25.00
Pt_{4ML}/Pd	9	16	144	75.00	25.00
Pt_{5ML}/Pd	9	16	144	75.00	25.00
Pt_{6ML}/Pd ($Pd_7@Pt_{3-U}$)	9	16	144	75.00	25.00
$Pt_{13}@Pt_{1ML}/Pd$	3	3	9		
	6	3	18		
	7	6	42		
	9	5	45		
	10	2	20		
	11	6	66		
			200	66.67	33.33
$Pt_{13}@Pt_{2ML}/Pd$	3	3	9		
	6	3	18		
	7	6	42		
	9	5	45		
	10	2	20		
	11	6	66		
($Pd_7@Pt_3$)			200	66.67	33.33

Note: Number of atoms on surface (No. atom), Number of metal coordination (No. CN), percentage of metal coordination (%CN), and percentage of metal undercoordination (%UN).

References

1. D. C. Marcano, D. V. Kosynkin, J. M. Berlin, A. Sinitskii, Z. Sun, A. Slesarev, L. B. Alemany, W. Lu and J. M. Tour, *ACS Nano*, 2010, **4**, 4806-4814.
2. D. C. Marcano, D. V. Kosynkin, J. M. Berlin, A. Sinitskii, Z. Sun, A. S. Slesarev, L. B. Alemany, W. Lu and J. M. Tour, *ACS Nano*, 2018, **12**, 2078−2078.
3. Y. Liu, A. Naseri, T. Li, A. Ostovan, E. Asadian, R. Jia, L. Shi, L. Huang and A. Z. Moshfegh, *ACS Appl. Mater. Interfaces*, 2022, **14**, 16527-16537.
4. B. Ravel and M. Newville, *J. Synchrotron Rad.*, 2005, **12**, 537-541.
5. S. I. Zabinsky, J. J. Rehr, A. Ankudinov, R. C. Albers and M. J. Eller, *Phys. Rev. B*, 1995, **52**, 2995-3009.
6. Z. Xia, H. Zhang, K. Shen, Y. Qu and Z. Jiang, *Physica B*, 2018, **542**, 12-19.
7. H. Yang, P. Guo, R. Wang, Z. Chen, H. Xu, H. Pan, D. Sun, F. Fang and R. Wu, *Adv. Mater.*, 2022, **34**, 2107548.
8. W. Zheng, *ACS Energy Lett.*, 2023, **8**, 1952-1958.
9. L. Yu and Z. Ren, *Materials Today Physics*, 2020, **14**, 100253.
10. K. Sun, T. Cheng, L. Wu, Y. Hu, J. Zhou, A. Maclennan, Z. Jiang, Y. Gao, W. A. Goddard, III and Z. Wang, *J. Am. Chem. Soc.*, 2017, **139**, 15608-15611.
11. P. Zhou, G. Hai, G. Zhao, R. Li, X. Huang, Y. Lu and G. Wang, *Appl. Catal. B Environ.*, 2023, **325**, 122364.
12. Y. Guo, D. Guo, F. Ye, K. Wang, Z. Shi, X. Chen and C. Zhao, *ACS Sustain. Chem. Eng.*, 2018, **6**, 11884-11891.
13. C. Tsounis, B. Subhash, P. V. Kumar, N. M. Bedford, Y. Zhao, J. Shenoy, Z. Ma, D. Zhang, C. Y. Toe, S. Cheong, R. D. Tilley, X. Lu, L. Dai, Z. Han and R. Amal, *Adv. Funct. Mater.*, 2022, **32**, 2203067.
14. G. Kresse and J. Furthmüller, *Phys. Rev. B*, 1996, **54**, 11169-11186.
15. S. Grimme, J. Antony, S. Ehrlich and H. Krieg, *The Journal of Chemical Physics*, 2010, **132**.
16. S. Grimme, *Journal of Computational Chemistry*, 2004, **25**, 1463-1473.
17. J. K. Nørskov, T. Bligaard, A. Logadottir, J. R. Kitchin, J. G. Chen, S. Pandelov and U. Stimming, *Journal of The Electrochemical Society*, 2005, **152**, J23.
18. D. R. Lide, *CRC handbook of chemistry and physics, 90th ed*, CRC Press/Taylor and Francis Group: Boca Raton, FL, 2010.
19. Y. Liu, Y. Ji, Q. Li, Y. Zhu, J. Peng, R. Jia, Z. Lai, L. Shi, F. Fan, G. Zheng, L. Huang and C. Li, *ACS Nano*, 2023, **17**, 15085-15096.
20. E. Pastor, F. M. Pesci, A. Reynal, A. D. Handoko, M. Guo, X. An, A. J. Cowan, D. R. Klug, J. R. Durrant and J. Tang, *Physical Chemistry Chemical Physics*, 2014, **16**, 5922-5926.
21. S. Pu, R. Zhu, H. Ma, D. Deng, X. Pei, F. Qi and W. Chu, *Appl. Catal. B Environ.*, 2017, **218**, 208-219.
22. X. Li, Y. Zhao, X. Wang, J. Wang, A. M. Gaskov and S. A. Akbar, *Sensors and Actuators B: Chemical*, 2016, **230**, 330-336.
23. Y. Zhou, Q. Bao, L. A. L. Tang, Y. Zhong and K. P. Loh, *Chem. Mater.*, 2009, **21**, 2950-2956.
24. I. K. Moon, J. Lee, R. S. Ruoff and H. Lee, *Nat. Commun.*, 2010, **1**, 73.
25. Y. Peng, J. Cao, J. Yang, W. Yang, C. Zhang, X. Li, R. A. W. Dryfe, L. Li, I. A. Kinloch and Z. Liu, *Adv. Funct. Mater.*, 2020, **30**, 2001756.
26. J. A. Quezada-Renteria, C. O. Ania, L. F. Chazaro-Ruiz and J. R. Rangel-Mendez, *Carbon*, 2019,

149, 722-732.
27. S.-Y. Pang, W.-F. Io and J. Hao, *Adv. Sci.*, 2021, **8**, 2102207.
28. M. Yi, N. Li, B. Lu, L. Li, Z. Zhu and J. Zhang, *Energy Storage Mater.*, 2021, **42**, 418-429.
29. W. Wang, Y. Wu, Y. Lin, J. Yao, X. Wu, C. Wu, X. Zuo, Q. Yang, B. Ge, L. Yang, G. Li, S. Chou, W. Li and Y. Jiang, *Adv. Funct. Mater.*, 2022, **32**, 2108464.
30. W.-H. Huang, X.-M. Li, D.-Y. Yu, X.-F. Yang, L.-F. Wang, P.-B. Liu and J. Zhang, *Nanoscale*, 2020, **12**, 19804-19813.
31. R. Du, W. Jin, R. Hübner, L. Zhou, Y. Hu and A. Eychmüller, *Adv. Energy Mater.*, 2020, **10**, 1903857.
32. L. Li, G. Zhang, B. Wang, T. Yang and S. Yang, *J. Mater. Chem. A.*, 2020, **8**, 2090-2098.
33. C. Zhang, Y. Cui, Y. Yang, L. Lu, S. Yu, Z. Meng, Y. Wu, Y. Li, Y. Wang, H. Tian and W. Zheng, *Adv. Funct. Mater.*, 2021, **31**, 2105372.
34. F. Luo, Q. Zhang, X. Yu, S. Xiao, Y. Ling, H. Hu, L. Guo, Z. Yang, L. Huang, W. Cai and H. Cheng, *Angew. Chem. Int. Ed.*, 2018, **57**, 14862-14867.
35. B. T. Jebaslinhepzybai, N. Prabu and M. Sasidharan, *Int. J. Hydrog. Energy*, 2020, **45**, 11127-11137.
36. Y. Yin, T. Liu, D. Liu, Z. Wang, Q. Deng, D. Qu, Z. Xie, H. Tang and J. Li, *J. Colloid Interface Sci.*, 2018, **530**, 595-602.
37. Q. Dang, Y. Sun, X. Wang, W. Zhu, Y. Chen, F. Liao, H. Huang and M. Shao, *Appl. Catal. B Environ.*, 2019, **257**, 117905.
38. B. Pang, X. Liu, T. Liu, T. Chen, X. Shen, W. Zhang, S. Wang, T. Liu, D. Liu, T. Ding, Z. Liao, Y. Li, C. Liang and T. Yao, *Energy Environ. Sci.*, 2022, **15**, 102-108.
39. Y. Li, S. Zhang, W. Xu, C. Jiang, L. Shao, S. Wang and J. Wang, *J. Mater. Chem. A.*, 2023, **11**, 4000-4006.
40. X. Cheng, Y. Lu, L. Zheng, Y. Cui, M. Niibe, T. Tokushima, H. Li, Y. Zhang, G. Chen, S. Sun and J. Zhang, *Nano Energy*, 2020, **73**, 104739.
41. F.-Y. Yu, Z.-L. Lang, L.-Y. Yin, K. Feng, Y.-J. Xia, H.-Q. Tan, H.-T. Zhu, J. Zhong, Z.-H. Kang and Y.-G. Li, *Nat. Commun.*, 2020, **11**, 490.
42. D. Kobayashi, H. Kobayashi, D. Wu, S. Okazoe, K. Kusada, T. Yamamoto, T. Toriyama, S. Matsumura, S. Kawaguchi, Y. Kubota, S. M. Aspera, H. Nakanishi, S. Arai and H. Kitagawa, *J. Am. Chem. Soc.*, 2020, **142**, 17250-17254.
43. D. Liu, X. Li, S. Chen, H. Yan, C. Wang, C. Wu, Y. A. Haleem, S. Duan, J. Lu, B. Ge, P. M. Ajayan, Y. Luo, J. Jiang and L. Song, *Nat. Energy*, 2019, **4**, 512-518.
44. M. Bao, I. S. Amiinu, T. Peng, W. Li, S. Liu, Z. Wang, Z. Pu, D. He, Y. Xiong and S. Mu, *ACS Energy Lett.*, 2018, **3**, 940-945.
45. L. Zhang, H. Liu, S. Liu, M. Norouzi Banis, Z. Song, J. Li, L. Yang, M. Markiewicz, Y. Zhao, R. Li, M. Zheng, S. Ye, Z.-J. Zhao, G. A. Botton and X. Sun, *ACS Catal.*, 2019, **9**, 9350-9358.
46. H. Zhang, P. Song, P. Yao, D. Zhang, J. Cao, X. Gong, C. Han and W. Xu, *Chem. Eng. J.*, 2023, **470**, 144375.
47. Y. Wu, W. Wei, R. Yu, L. Xia, X. Hong, J. Zhu, J. Li, L. Lv, W. Chen, Y. Zhao, L. Zhou and L. Mai, *Adv. Funct. Mater.*, 2022, **32**, 2110910.
48. Y. Guo, B. Hou, X. Cui, X. Liu, X. Tong and N. Yang, *Adv. Energy Mater.*, 2022, **12**, 2201548.
49. L. Zhang, L. Han, H. Liu, X. Liu and J. Luo, *Angew. Chem. Int. Ed.*, 2017, **56**, 13694-13698.
50. K. Jiang, B. Liu, M. Luo, S. Ning, M. Peng, Y. Zhao, Y.-R. Lu, T.-S. Chan, F. M. F. de Groot

and Y. Tan, *Nat. Commun.*, 2019, **10**, 1743.

51. K. L. Zhou, Z. Wang, C. B. Han, X. Ke, C. Wang, Y. Jin, Q. Zhang, J. Liu, H. Wang and H. Yan, *Nat. Commun.*, 2021, **12**, 3783.
52. J. Yan, Z. Xi, L. Cong, K. Lv, R. Xin, B. Cao, B. Liu, J. He and J. Zhang, *Small*, 2022, **18**, 2205603.
53. N. Nie, D. Zhang, Z. Wang, W. Yu, S. Ge, J. Xiong, Y. Gu, B. Yang, J. Lai and L. Wang, *Appl. Catal. B Environ.*, 2022, **318**, 121808.
54. Z. Wu, Y. Zhao, W. Xiao, Y. Fu, B. Jia, T. Ma and L. Wang, *ACS Nano*, 2022, **16**, 18038-18047.
55. L. Zhai, X. She, L. Zhuang, Y. Li, R. Ding, X. Guo, Y. Zhang, Y. Zhu, K. Xu, H. J. Fan and S. P. Lau, *Angew. Chem. Int. Ed.*, 2022, **61**, e202116057.
56. Y. Tian, M. Wen, A. Huang, Q. Wu, Z. Wang, Q. Zhu, T. Zhou and Y. Fu, *Small*, 2023, **19**, 2207569.
57. X. Cheng, B. Xiao, Y. Chen, Y. Wang, L. Zheng, Y. Lu, H. Li and G. Chen, *ACS Catal.*, 2022, **12**, 5970-5978.
58. J. Cai, X. Liao, P. Li, Q. Wang, H. Huang, Z. Lyu, J. Lin and S. Xie, *Chem. Eng. J.*, 2022, **429**, 132414.
59. J. Kim, H. Kim, W.-J. Lee, B. Ruqia, H. Baik, H.-S. Oh, S.-M. Paek, H.-K. Lim, C. H. Choi and S.-I. Choi, *J. Am. Chem. Soc.*, 2019, **141**, 18256-18263.
60. J. Lu, P.-J. Deng, A. Chen, C. Yang, H. Zhu and H.-P. Liang, *J. Mater. Chem. A.*, 2023, **11**, 2452-2459.